UNIVERSITÀ DEGLI STUDI DI PADOVA

Dipartimento di Fisica e Astronomia “Galileo Galilei”

Corso di Laurea Magistrale in Fisica

Tesi di Laurea

Stabilization of the squeezed vacuum source for the Virgo interferometer

Relatore
Prof. Jean-Pierre Zendri
Correlatore
Dr. Marco Vardaro

Laureando
Fabio Bergamin

Anno Accademico 2017/2018

Contents

Abstract

In this thesis an alternative method to stabilize the phase of a squeezed vacuum field in the framework of the Virgo gravitational wave detector is designed and realized. A brief introduction about the nature of gravitational waves and their detection is presented in chapter 1, with particular attention to the actual sensitivity limitations on the interferometers employed. Chapter 2 focuses on the quantum nature of the electromagnetic field. A nonclassical state of the light, the squeezed state, is described, as well as how it is is produced and how can be observed. This kind of radiation field is employed to increase the sensitivity of the detectors beacause with its injection into the interferometer the quantum noise that affects the measure is partially reduced. In order to avoid any technical noise contamination, a second copropagating and frequency shifted field is used to provide the error signal for the alignment and to allow the phase locking between the interferometer main laser and the squeezed light, as discussed in chapter 3, where the technique called *coherent control loop* is explained. Finally, in chapter 4, the optical bench and the control electronics realized at LNL to test the stability of the control loop are presented; the system will be implemented in Virgo in the next months. The difference between the method discussed here and that usually employed is that the error signal is not used to correct the path of the squeezed vacuum field, but it is instead used to close a cascade loop on a PLL. Thus all the actuators are electronic and no optical actuators are used, the stray light issue is minimized. The control loop is stronger at low frequencies in order to correct the seismic noise that dominates in this region.

Chapter 1

Introduction

1.1 Gravitational Waves

When one wants to talk about gravitation, it is cardinal to begin with the Einstein equations, which define the relation between space-time geometry and energetic content:

$$R_{\mu\nu} - \frac{1}{2} g_{\mu\nu} R = \frac{8\pi G}{c^4} T_{\mu\nu} \tag{1.1}$$

where $R_{\mu\nu}$ is the Ricci tensor, $R = g_{\mu\nu} R^{\mu\nu}$ is the Ricci scalar, $g_{\mu\nu}$ is the curved space-time metric, G is the universal gravitational constant, c is the speed of light in a vacuum and $T_{\mu\nu}$ is the energy-momentum tensor. A perturbative approach can se used [Mag07, §1.1,§1.2] by linearizing the metric around the Minkowski flat space-time metric $\eta_{\mu\nu}$ as follows:

$$g_{\mu\nu} = \eta_{\mu\nu} + h_{\mu\nu}, \qquad |h_{\mu\nu}| \ll 1. \tag{1.2}$$

By substituting (1.2) in (1.1) and solving in a vacuum ($T_{\mu\nu} = 0$), after some algebra we obtain

$$\Box \bar{h}_{\mu\nu} = 0. \tag{1.3}$$

$\Box = \partial_\mu \partial^\mu = \boldsymbol{\nabla}^2 - \partial_t^2 / c^2$ is the flat space d'Alembertian, so (1.3) is the wave equation for $\bar{h}_{\mu\nu}$, the tensor defined as:

$$\bar{h}_{\mu\nu} \equiv h_{\mu\nu} - \frac{1}{2} \eta_{\mu\nu} h^{\sigma}_{\sigma}. \tag{1.4}$$

To write (1.3) in such a simple form, we have choosen the Lorentz gauge

$$\partial^\nu \bar{h}_{\mu\nu} = 0. \tag{1.5}$$

Solutions of (1.3) are gravitational waves (GW) which propagate at the speed of light c. Choosing the transverse-traceless gauge, they can be written as:

$$h_{\mu\nu}(z,t) = \begin{pmatrix} 0 & 0 & 0 & 0 \\ 0 & h_+ & h_\times & 0 \\ 0 & h_\times & -h_+ & 0 \\ 0 & 0 & 0 & 0 \end{pmatrix} \cos\left(2\pi f\left(t - \frac{z}{c}\right)\right) \tag{1.6}$$

where we are considering planar waves propagating through the z-direction. Note that having chosen a traceless gauge ($h^\sigma_\sigma = 0$) there is no more difference between $h_{\mu\nu}$ and $\bar{h}_{\mu\nu}$. The number of independent components of the metric is two, corresponding to different polarizations of the transverse wave h_+ and $h_\times$. The effects on matter are illustrated in Fig. 1.1, where the waves enter perpendicular to the plane.

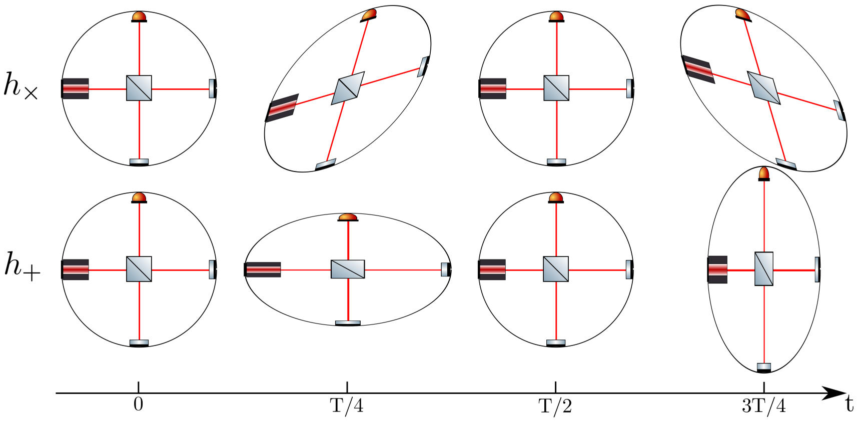

FIGURE 1.1: Effects of GW passing through an ITF with different polarizations. T is the period of the waves.

1.2 Gravitational Wave Detectors

Earth-based detectors make use of the Michelson interferometer (ITF) (Fig. 1.2), which purpose is to transform an optical phase modulation signal into an amplitude modulation which can be measured by a single photodiode (PD). Continuous wave light from a laser is divided into two beams with a beamsplitter (BS), the beams then travel along the two perpendicular arms of the ITF and are reflected back to the BS where they interfere and are directed to the PD, which converts the intensity into an electric signal. Any change in the optical path difference between the arms results in a change in the interference signal: a GW of frequency f passing through the ITF will produce an electric signal at the same frequency. The output power, proportional to the square

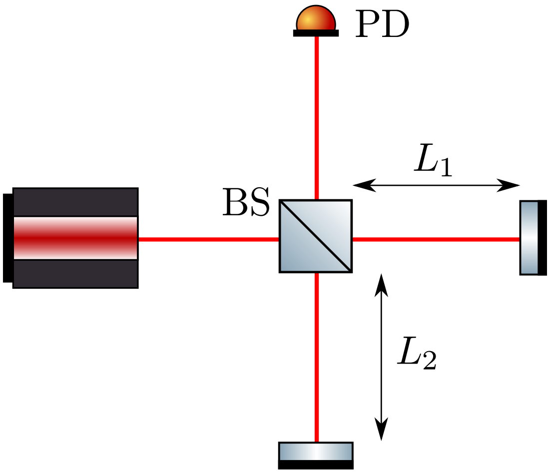

FIGURE 1.2: Basic setup of a Michelson ITF

of the radiation field, is given by:

$$P_{out} = P_{in} \cos^2[k(L_1 - L_2)] \tag{1.7}$$

where beams propagating in a vacuum are considered; k is the wavenumber, and L_1 and L_2 are the arm lengths. It is important that the two end mirrors are mounted onto free masses in order to detect only gravitational effects, thus they are suspended and placed in a multiple stage pendulum with resonance frequency lower than detector sensitivity bandwidth.

Assume that a monochromatic GW with frequency f and polarization h_+ has to be detected, like that illustrated at the bottom of Fig. 1.1; for simplicity, from here on, we will consider an ITF with equal length of the arms L. The metric perturbation (1.6) is simply:

$$h_{\mu\nu}(t) = \begin{pmatrix} 0 & 0 & 0 & 0 \\ 0 & 1 & 0 & 0 \\ 0 & 0 & -1 & 0 \\ 0 & 0 & 0 & 0 \end{pmatrix} h(t) \tag{1.8}$$

where

$$h(t) = h_+ \cos\left(2\pi f \left(t - \frac{z}{c}\right)\right) \tag{1.9}$$

is the *strain* of the GW. When passing through the detector, the GW stretches out an arm by a certain amount $\delta L(t)$ and squeezes the other arm by the same amount periodically. The strain is related to elongation $\delta L(t)$ by:

$$h(t) \equiv 2\frac{\delta L(t)}{L}. \tag{1.10}$$

Considering only gravitational effects, the output power becomes

$$P_{out}(t) = P_{in}\cos^2[k((L+\delta L(t)) - (L - \delta L(t)))] \quad (1.11)$$

$$= P_{in}\cos^2[kLh(t)], \quad (1.12)$$

with a Michelson ITF we are hence able to obtain $h(t)$ from a measure of $P_{out}(t)$. The performance of a detector is given by the frequency-dependent noise that limits its sensitivity; for stochastic noise, the linear spectral density is used, which is the square root of the power spectral density[1] of $h(t)$ noise: $\sqrt{S_{hh}(f)}[1/\sqrt{Hz}]$.

1.3 Noise Budget

Many sources of noise affect the sensibility of a gravitational ITF [AD05]; Fig. 1.3 shows the sensitivity curve with the solely contribution of ambient noise. With several efforts to isolate the system, the noise arising from the quantum nature of light is the limiting noise source over most of the audio GW detection band. This noise consists in the unavoidable fluctuations in conjugate variables such as the quadratures of the radiation field (see §2.1.1), and is the quadrature sum of two contributions, as explained below.

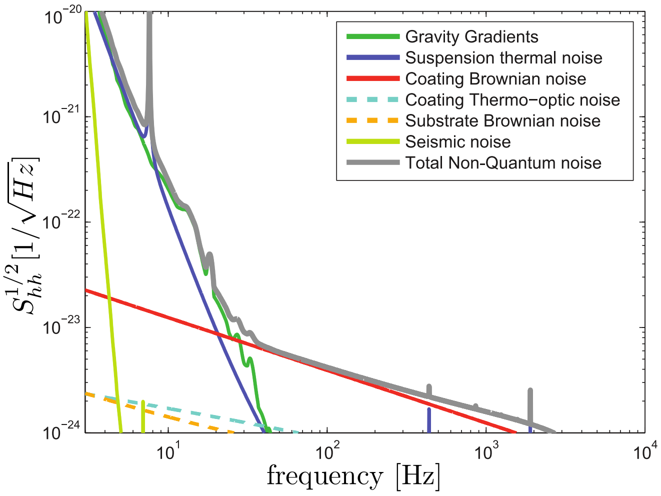

FIGURE 1.3: Non-quantum noise limiting sources to AdV sensitivity.

---

[1] the power spectral density of a weak-sense stationary process $x(t)$ is defined as $S_{XX}(\omega) \equiv \langle X(\omega)X^*(\omega)\rangle$, where $X(\omega)$ is the Fourier transform of $x(t)$

1.3.1 Shot Noise

This type of noise arises from the fluctuations of the Poissonian counting statistics of a coherent state of light (see §2.2.1). When the radiation coming from the ITF is revealed by the PD, fluctuations in the number of photons could be interpreted as a fringe shift, resulting in a false signal for the detector.
The shot noise contribution to the linear spectral density is given by [Sau94, §5.1]:

$$S_{hh}^{1/2}\Big|_{s.n.} = \frac{1}{L}\sqrt{\frac{\hbar c\lambda}{2\pi P}}. \tag{1.13}$$

where L is the arm length of the ITF, λ is the wavelength of the laser and P its power. From (1.13) it is clear that an increase in the laser power leads to a reduction of the shot noise; another important aspect is that it doesn't depend on wave frequency to be detected: it is white noise.

1.3.2 Radiation Pressure Noise

When a photon of energy $\hbar\omega$ bounces on a surface, it transfers a momentum of $2\hbar\omega/c$ to that surface . Fluctuations in photon number lead to fluctuations in the pressure acting on the mirrors of the ITF and generate a stochastic force that shakes them.
The shot noise contribution to the linear spectral density of the GW strain amplitude is given by [Sau94, §5.2]:

$$S_{hh}^{1/2}(f)\Big|_{r.p.} = \frac{2}{m(2\pi f)^2 L}\sqrt{\frac{2\pi\hbar P}{c\lambda}} \tag{1.14}$$

where m is the mass of the mirror and f the frequency at which it oscillates. From its dependence on f, it is clear that this contribution to the total noise is dominant at low frequencies.

1.3.3 Standard Quantum Limit

The total quantum noise is given by the sum in quadrature of the contributions discussed above:

$$S_{hh}^{1/2}(f)\Big|_{q.n.} = \sqrt{S_{hh}|_{s.n.} + S_{hh}(f)|_{r.p.}}. \tag{1.15}$$

For a fixed frequency we can minimize the above equation with respect to the power and, at optimal power, we find:

$$S_{hh}^{1/2}(f)\Big|_{s.q.l.} = \frac{1}{\pi f L}\sqrt{\frac{\hbar}{m}} \tag{1.16}$$

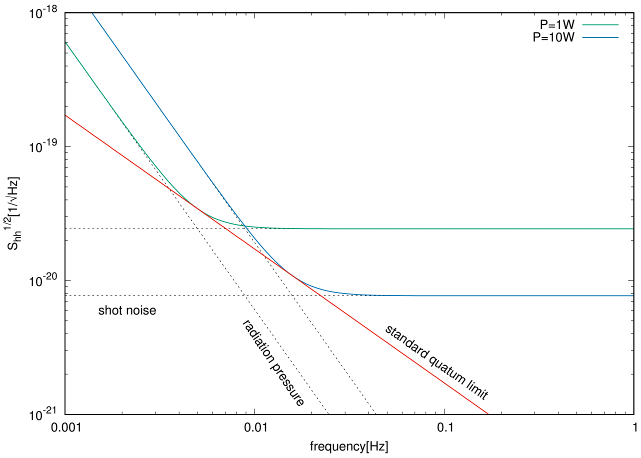

FIGURE 1.4: Linear spectral density of the strain noise for different values of the laser power. The parameters are assumed to be $m = 40kg$, $\lambda = 1064nm$, $L = 3km$.

for an optimal value of the power given by:

$$P_{opt} = \pi c \lambda m f^2. \tag{1.17}$$

In Fig. 1.4 linear spectral densities for two values of the laser power are plotted. The standard quantum limit represents a lower limit for the spectral density of the quantum noise, it is not a spectral density but it is rather the locus of the lowest possible points of the family of spectra. For this reason, (1.16) is sometimes called a "pseudo-spectral density".

By substituting realistic parameters in P_{opt}, such as $\lambda = 1064nm$, $f = 100Hz$[2] and $m = 40kg$, we find an extremely large value for the power. Even if we were to consider *folded* ITFs, i.e. with a Fabry-Pérot cavity along each arm (see Fig. 1.5), for which the optimum power takes the form [Sau94, §6.8]

$$P_{opt} = \frac{\pi c \lambda m f^2}{2\mathcal{N}^2} \tag{1.18}$$

where $\mathcal{N}$ is the number of bounces at each mirror, we would find $P_{opt} \simeq 5kW$ for $\mathcal{N} = 200$. This is too high a power for today's continuous wave lasers, thus we can see that the dominant contribution to the quantum noise is given by the shot noise. The introduction of optical cavities along the arms of the ITF enhances the sensitivity to a phase shift by a factor $2\mathcal{F}/\pi$ [Mag07, §9.2], where $\mathcal{F}$ is the *finesse* of the cavity and is proportional to $\mathcal{N}$. The reason of this improvement is that photons bounce many times between the two mirrors and hence they experience a longer storage time: the effective optical path can be increased by a factor of $\mathcal{O}(10^2)$ with the appropriate choice of mirror reflectivity. The finesse, however, cannot be augmented arbitrarily

---

[2] Detection band of Earth-based GW detectors is from about 10 Hz to 10 kHz

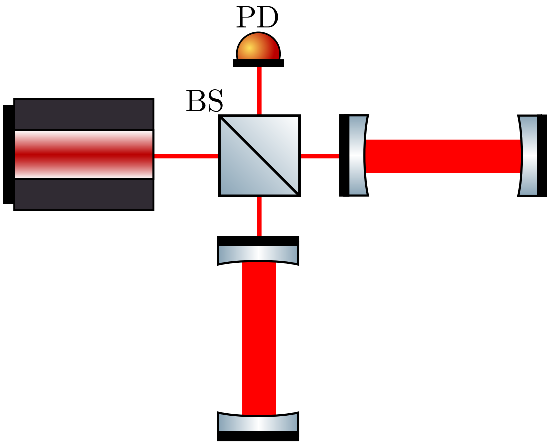

FIGURE 1.5: Michelson ITF with Fabry-Pérot cavities along the arms

because over certain values the sensitivity at high frequency get worse. This behaviour arises from the fact that in a folded ITF the shot noise depends on the frequency f as

$$\frac{1}{\sqrt{1+(f/f_p)^2}} \tag{1.19}$$

where $f_p \simeq c/(4\pi\mathcal{F})$ is the so-called pole frequency. The injection of a frequency independent squeezed vacuum through the dark port of the ITF (see §2.3) allows the reduction of one of the two contributions to the quantum noise, depending on the squeezing angle. Below $100Hz$, the quantum noise level and non-quantum noise level are of the same order of magnitude; thus it makes sense to reduce the shot noise, which is dominant at high frequencies, at the price of a higher pressure noise at low frequencies, the contribution of which being covered by ambient noise.

Chapter 2

Quantum Theory of Light

This chapter briefly presents the mathematical tools needed to describe the radiation field in the context of the second quantization of light. We assume that the reader is familiar with the concepts of quantum harmonic oscillator and Fock states. A simple introduction to the argument can be found in [Sal14, pp. 21–32].

2.1 Quantized Electromagnetic Field

Elaborating upon Maxwell's equations in a vacuum and without sources, the coupled quantized electric and magnetic fields can be described respectively with:

$$\hat{\boldsymbol{E}} = \sum_{\boldsymbol{k},s} i\sqrt{\frac{\hbar\omega_k}{2\varepsilon_0 V}} \left(\hat{a}_{\boldsymbol{k},s} e^{-i(\omega_k t - \boldsymbol{k}\cdot\boldsymbol{r})} - \hat{a}^\dagger_{\boldsymbol{k},s} e^{i(\omega_k t - \boldsymbol{k}\cdot\boldsymbol{r})}\right) \boldsymbol{\epsilon}_{\boldsymbol{k},s} \tag{2.1}$$

$$\hat{\boldsymbol{B}} = \sum_{\boldsymbol{k},s} i\sqrt{\frac{\hbar}{2\varepsilon_0 \omega_k V}} \left(\hat{a}_{\boldsymbol{k},s} e^{-i(\omega_k t - \boldsymbol{k}\cdot\boldsymbol{r})} - \hat{a}^\dagger_{\boldsymbol{k},s} e^{i(\omega_k t - \boldsymbol{k}\cdot\boldsymbol{r})}\right) \boldsymbol{k} \times \boldsymbol{\epsilon}_{\boldsymbol{k},s} \tag{2.2}$$

where $\hbar$ is the reduced Planck constant, ω_k is the mode angular frequency, $\boldsymbol{k}$ is the wavevector such that $\omega_k = c|\boldsymbol{k}|$ with c being the speed of light in a vacuum, $s = 1, 2$ is the polarization, ε_0 is the vacuum permittivity, V is the volume in which the plane waves are normalized, $\boldsymbol{\epsilon}_{\boldsymbol{k},1}$ and $\boldsymbol{\epsilon}_{\boldsymbol{k},2}$ are two mutually orthogonal real unit vectors of polarization which are also orthogonal to $\boldsymbol{k}$, and $\hat{a}_{\boldsymbol{k},s}$ and $\hat{a}^\dagger_{\boldsymbol{k},s}$ are respectively the boson annihilation and creation operators.

For simplicity, below we will only deal with the electric field operator[1] and we will consider it in a single mode and with a fixed linear polarization. With these assumptions

---

[1] from classical electromagnetism theory, we know that electric and magnetic fields are perpendicular to each other and to the wavevector, and that their amplitudes are related by $B = E/c$

(2.1) can be rewritten as

$$\hat{\boldsymbol{E}} = \sqrt{\frac{\hbar\omega_k}{2\varepsilon_0 V}} \left(\hat{a} e^{-i\left(\omega_k t - \boldsymbol{k}\cdot\boldsymbol{r} - \frac{\pi}{2}\right)} + \hat{a}^\dagger e^{i\left(\omega_k t - \boldsymbol{k}\cdot\boldsymbol{r} - \frac{\pi}{2}\right)}\right) \boldsymbol{\epsilon}. \tag{2.3}$$

2.1.1 Quadrature Operators

Creation and annihilation operators are not associated with observable quantities because they are not Hermitian; in order to handle observable quantities, we introduce *amplitude* and *phase quadrature operators*:

$$\hat{X} = \frac{1}{2}(\hat{a} + \hat{a}^\dagger) \tag{2.4}$$

$$\hat{Y} = \frac{1}{2i}(\hat{a} - \hat{a}^\dagger) \tag{2.5}$$

in terms of which the electric field operator (2.3) may be rewritten as

$$\hat{\boldsymbol{E}} = 2\sqrt{\frac{\hbar\omega_k}{2\varepsilon_0 V}} \left(\hat{X}\cos\left(\omega_k t - \boldsymbol{k}\cdot\boldsymbol{r} - \frac{\pi}{2}\right) + \hat{Y}\sin\left(\omega_k t - \boldsymbol{k}\cdot\boldsymbol{r} - \frac{\pi}{2}\right)\right) \boldsymbol{\epsilon}. \tag{2.6}$$

Any pair of quadrature operators could be obtained by applying the rotation matrix of angle χ on the $(\hat{X}, \hat{Y})$ vector:

$$\hat{X}_\chi = \hat{X}\cos\chi + \hat{Y}\sin\chi = \frac{1}{2}(\hat{a}e^{-i\chi} + \hat{a}^\dagger e^{i\chi}) \tag{2.7}$$

$$\hat{Y}_\chi = \hat{X}_{\chi+\frac{\pi}{2}} = \hat{X}(-\sin\chi) + \hat{Y}\cos\chi = \frac{1}{2i}(\hat{a}e^{-i\chi} - \hat{a}^\dagger e^{i\chi}). \tag{2.8}$$

From the commutation relation of $\hat{a}$ ad $\hat{a}^\dagger$:

$$[\hat{a}, \hat{a}^\dagger] = 1, \tag{2.9}$$

it could be easily verified that the quadrature operators do not commute:

$$[\hat{X}_\chi, \hat{Y}_\chi] = \frac{i}{2}. \tag{2.10}$$

Thus, they obey the Heisenberg uncertainty principle [Hei27]:

$$\langle \Delta\hat{X}_\chi^2\rangle\langle\Delta\hat{Y}_\chi^2\rangle \geq \frac{1}{16}. \tag{2.11}$$

2.2 Quantum States of Light

Fock states are not ideal to describe real fields, since the mean value of the electric field operator described in (2.3):

$$\langle \hat{\boldsymbol{E}} \rangle_n \equiv \langle n | \hat{\boldsymbol{E}} | n \rangle = \mathbf{0} \tag{2.12}$$

is zero regardless of the number of photons, as a consequence of the completely undefined phase of these states [Fox06, p. 139].

2.2.1 Coherent States

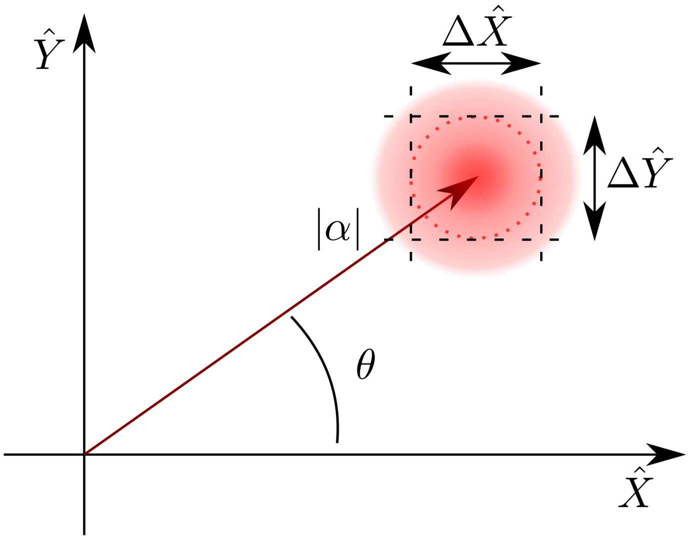

Figure 2.1: Phasor diagram of a coherent state. The time evolution of the electric field in such a state could be visualized considering the projections of the phasor and its uncertainty circle on a complex plane with axes $\hat{E}$ and $\dot{\hat{E}}$ rotating with angular frequency ω relative to the (X, Y) plane

A set of states better suited to describe a real field, like that generated by a laser device, is given by the eigenstates of the annihilation operator [Gla63]

$$\hat{a} \, |\alpha\rangle = \alpha \, |\alpha\rangle \tag{2.13}$$

where $\alpha = |\alpha| e^{i\theta}$ is a complex number; Roy Glauber named such states *coherent states*. With this choice of states, the expectation value of the electric field is

$$\langle \hat{\boldsymbol{E}} \rangle_\alpha \equiv \langle \alpha | \hat{\boldsymbol{E}} | \alpha \rangle = 2|\alpha| \sqrt{\frac{\hbar \omega_k}{2\varepsilon_0 V}} \sin(\omega_k t - \boldsymbol{k} \cdot \boldsymbol{r} - \theta) \boldsymbol{\epsilon} \tag{2.14}$$

which resembles the classical description of a coherent monocromatic electromagnetic wave. From (2.14) we see that the absolute value of the eigenvalue of (2.13) is proportional to the amplitude of the electric field, while its phase enters in the sine of (2.14). Furthermore, we observe that if we invert (2.4) and (2.5) and we take the mean value of the operators involved with the system in the state $|\alpha\rangle$, we obtain:

$$\langle\hat{a}\rangle_\alpha = \langle\hat{X}\rangle_\alpha + i\langle\hat{Y}\rangle_\alpha; \tag{2.15}$$

the Hermitian quadrature operators can thus be interpreted as the real and imaginary part of the annihilation operator. With these considerations, we can represent the state $|\alpha\rangle$ as a phasor of length $|\alpha|$ at angle θ in the (X, Y) plane [Fox06, §7.5]; see Fig. 2.1. The red circle represents the quantum fluctuatuions which have a gaussian distribution around the mean value [BR04, §4.3.2] and are uniformly distributed in every field quadrature:

$$\langle\Delta\hat{X}_\chi^2\rangle_\alpha = \frac{1}{4} \qquad \forall\chi. \tag{2.16}$$

The above statement has an important implication: a coherent state is a state of minimum uncertainty, like the ground state of a harmonic oscillator, in fact for every couple of conjugate variable holds the identity:

$$\langle\Delta\hat{X}_\chi^2\rangle\langle\Delta\hat{Y}_\chi^2\rangle = \frac{1}{16}. \tag{2.17}$$

Let us now calculate calculate the mean value of the number operator:

$$\bar{N} = \langle\alpha|\hat{N}|\alpha\rangle = |\alpha|^2 \tag{2.18}$$

and its variance:

$$\langle\Delta\hat{N}^2\rangle = \langle\hat{N}^2\rangle - \langle\hat{N}\rangle^2 = \bar{N}^2. \tag{2.19}$$

The probability of measuring n photons in a coherent state $|\alpha\rangle$ is

$$P(n) = |\,\langle n|\alpha\rangle\,| = e^{-|\alpha|^2}\frac{|\alpha|^{2n}}{n!} = e^{-\bar{N}}\frac{\bar{N}^n}{n!} \tag{2.20}$$

which is the Poisson distribution. A coherent state can be obtained by applying the *displacement operator*

$$\hat{D}(\alpha) = e^{\alpha\hat{a}^\dagger - \alpha^*\hat{a}} \tag{2.21}$$

to the vacuum state of the Fock space:

$$|\alpha\rangle = \hat{D}(\alpha)\,|0\rangle\,. \tag{2.22}$$

The displacement operator is unitary:

$$\hat{D}^\dagger(\alpha)\hat{D}(\alpha) = \mathbb{1} \tag{2.23}$$

and acts on $\hat{a}$ and $\hat{a}^\dagger$ as:

$$\hat{D}^\dagger(\alpha)\hat{a}\hat{D}(\alpha) = \hat{a} + \alpha \tag{2.24}$$

$$\hat{D}^\dagger(\alpha)\hat{a}^\dagger\hat{D}(\alpha) = \hat{a}^\dagger + \alpha^*. \tag{2.25}$$

2.2.2 Squeezed Vacuum

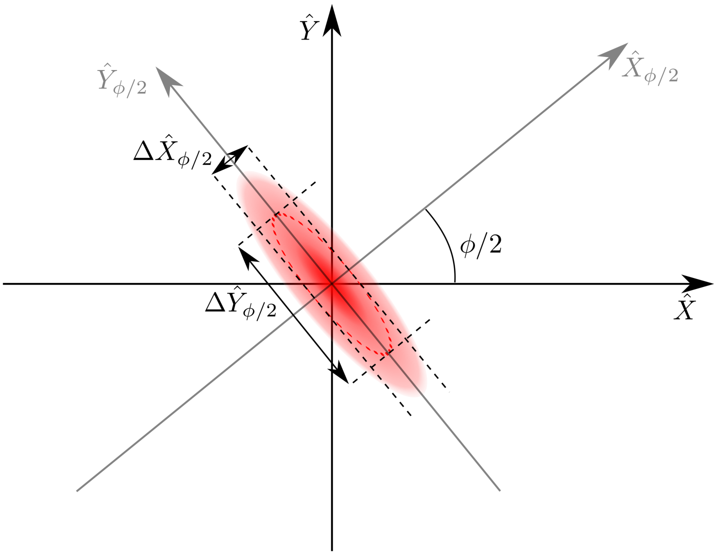

Figure 2.2: Phasor diagram of a squeezed vacuum state

A quantum state of light which–as opposed to a coherent state–has no classical counterpart is the *squeezed vacuum*, obtained by applying the *squeezing operator* [Sto70]

$$\hat{S}(\zeta) = e^{\frac{1}{2}(\zeta^*\hat{a}^2 - \zeta(\hat{a}^\dagger)^2)} \tag{2.26}$$

to the vacuum state

$$|\zeta\rangle = \hat{S}(\zeta)\,|0\rangle\,. \tag{2.27}$$

The complex number ζ can be written as

$$\zeta = re^{i\phi} \tag{2.28}$$

where r and ϕ are respectively called *squeezing factor* and *squeezing angle*. Similarly to what done in the previous section, we can depict a squeezed vacuum in a phase space as illustrated in Fig. 2.2. The expectation value of the generic quadrature operator is

$$\langle \hat{X}_\chi \rangle_\zeta = 0 \tag{2.29}$$

and the relative variance is given by:

$$\langle \Delta \hat{X}_\chi^2 \rangle_\zeta = \frac{1}{4}\left(\cosh^2 r + \sinh^2 r - 2\sinh r \cosh r \cos(\phi - 2\chi)\right) \tag{2.30}$$

Fig. (2.3) shows the variance of the quadrature operator with rispect to the variance of the coherent vacuum as a function of the quadrature angle for different values of the squeezing factor, the function has a periocity of π. The minimum and maximum value of (2.30) are reached for the two orthogonal quadrature rotated at half the squeezing angle, called respectively squeezed and anti-squeezed quadrature:

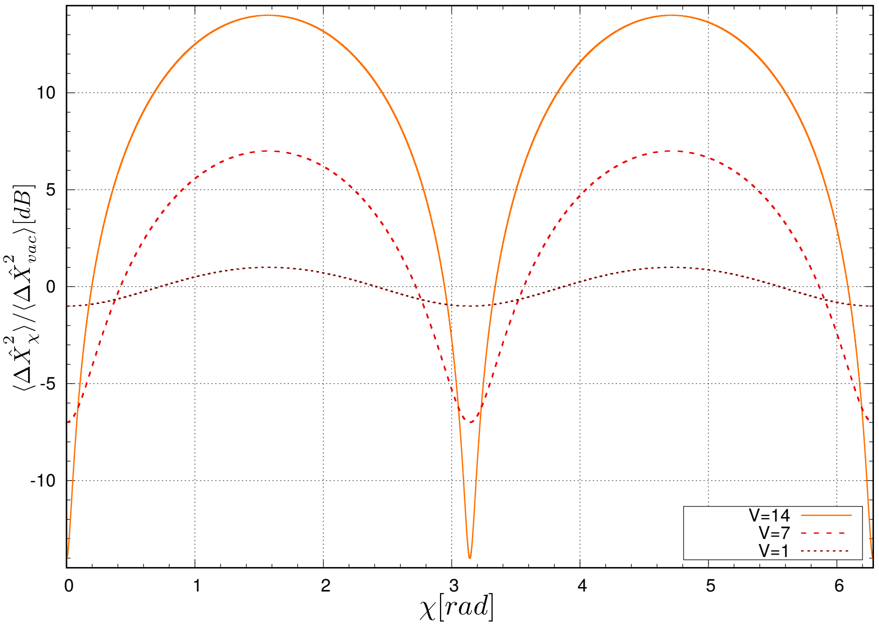

FIGURE 2.3: Quadrature noise of a squeezed vacuum with squeezing angle $\phi = 0$ as a function of the quadrature angle χ for various values of squeezing factor r.

$$\langle \Delta \hat{X}_{\phi/2}^2 \rangle_\zeta = \frac{e^{-2r}}{4} \tag{2.31}$$

$$\langle \Delta \hat{Y}_{\phi/2}^2 \rangle_\zeta = \frac{e^{2r}}{4}. \tag{2.32}$$

From the last equations we can understand the meaning of the name given to states like $|\zeta\rangle$: the quantum noise of a field quadrature is "squeezed" to respect the noise of the vacuum state, while the noise of the perpendicular quadrature is greater than that of the vacuum. The squeezing level V is often given in decibel scale using the transformation [Kha11, (2.118)]

$$V[dB] = -10\log_{10}\left(\frac{\langle \Delta \hat{X}^2_{\phi/2}\rangle}{\langle \Delta \hat{X}^2_{vac}\rangle}\right) = -10\log_{10}(e^{-2r}) \tag{2.33}$$

where $\langle \Delta \hat{X}^2_{\phi/2}\rangle$ is the variance lower noise quadrature and $\langle \Delta \hat{X}^2_{vac}\rangle$ is the variance of any quadrature of the coherent vacuum state.

The squeezed vacuum is still a minimum uncertainty state:

$$\langle \Delta \hat{X}^2_{\phi/2}\rangle_\zeta \langle \Delta \hat{Y}^2_{\phi/2}\rangle_\zeta = \frac{1}{16} \tag{2.34}$$

The squeezing operator is unitary and acts on $\hat{a}$ and $\hat{a}^\dagger$ as [Lou00, p. 202]:

$$\hat{S}^\dagger(\zeta)\hat{a}\hat{S}(\zeta) = \hat{a}\cosh r - \hat{a}^\dagger e^{i\phi}\sinh r \tag{2.35}$$

$$\hat{S}^\dagger(\zeta)\hat{a}^\dagger\hat{S}(\zeta) = \hat{a}^\dagger\cosh r - \hat{a} e^{-i\phi}\sinh r. \tag{2.36}$$

Despite its name, the squeezed vacuum has non-trivial photon statistics and could be described as a superposition of Fock (even) number states [GK04, pp. 160–161]:

$$|\zeta\rangle = \frac{1}{\sqrt{\cosh r}}\sum_{m=0}^{\infty}(-1)^m\frac{\sqrt{(2m)!}}{2^m m!}e^{im\phi}(\tanh r)^m\,|2m\rangle\,. \tag{2.37}$$

As a result, the mean value of number of photons in a squeezed vacuum is

$$\langle\zeta|\hat{N}|\zeta\rangle = \sinh^2 r \tag{2.38}$$

in contrast to the ground state $|0\rangle$ which has a mean value of zero photons.

2.3 Improvement of ITF Sensibility

In the present section we see how the injection of squeezed vacuum in the dark port[2] of the ITF can reduce the quantum noise, in doing this we will follow the reasoning of Caves [Cav81], who first demonstrated that the quantum noise in GW detectors is dominated by the vacuum fluctuations that enter the unused port of the ITF. The basic setup to introduce the squeezed vacuum in the ITF is depicted in Fig. 2.4: the squeezed field enters the ITF after it has been reflected by a polarized beam splitter (PBS), then a Faraday rotator changes the polarization direction of 45°. When the field comes back

---

[2] the dark port is the face of the BS from which the ITF laser beam exits.

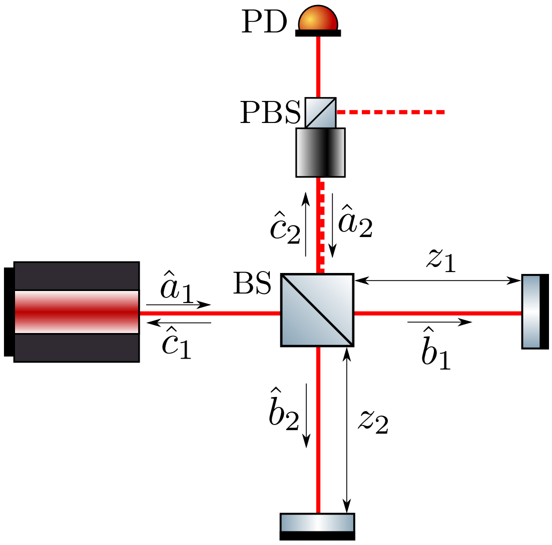

Figure 2.4: Scheme of the ITF with the squeezed vacuum injected in the unused port

from the ITF arms the rotator changes again the polarization direction so that the field outgoing from it has a polarization orthogonal to that of the original squeezed vacuum and is thus transmitted by the PBS toward the PD. The final polarization of the squeezed vacuum must be equal to that of the main laser circulating in the ITF in order to have a coupling of the two fields.

2.3.1 Beam Splitter

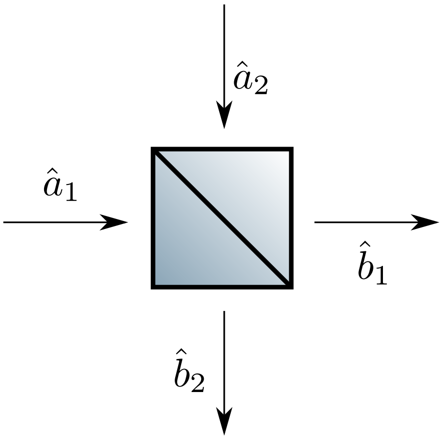

Figure 2.5: Quantum mechanical depiction of a BS

To describe the BS in a quantum mechanical way, we replace the classical complex field amplitudes with the correspondent annihilation operators as depicted in Fig. 2.5, where $\hat{a}_1$ and $\hat{a}_2$ are referred to the input fields and $\hat{b}_1$ and $\hat{b}_2$ to the output fields. It is worth noting that while in the classical description of the device it could be possible to consider only one input field, when we introduce the quantum operators we are forced to consider both the input quantized fields, substituting the unused port field with the vacuum state if necessary. As explained in [GK04, p. 138], this constraint arises from the boson commutation relations that the mode operators must satisfy:

$$[\hat{a}_i, \hat{a}_j^\dagger] = \delta_{ij} \tag{2.39}$$

$$[\hat{b}_i, \hat{b}_j^\dagger] = \delta_{ij} \tag{2.40}$$

$$[\hat{a}_i, \hat{a}_j] = [\hat{a}_i^\dagger, \hat{a}_j^\dagger] = [\hat{b}_i, \hat{b}_j] = [\hat{b}_i^\dagger, \hat{b}_j^\dagger] = 0. \tag{2.41}$$

We can use a complex matrix M_{BS} to represent the transformation of the BS acting on the annihilation operators of the input fields at a chosen angular frequency:

$$\begin{pmatrix} \hat{b}_1 \\ \hat{b}_2 \end{pmatrix} = M_{\mathrm{BS}} \begin{pmatrix} \hat{a}_1 \\ \hat{a}_2 \end{pmatrix} = \begin{pmatrix} t & r \\ r' & t' \end{pmatrix} \begin{pmatrix} \hat{a}_1 \\ \hat{a}_2 \end{pmatrix} \tag{2.42}$$

where r and r' are the reflective coefficients and t and t' are the transmission coefficients. By imposing the photon number (and hence the energy) conservation in a lossless BS:

$$\hat{b}_1^\dagger \hat{b}_1 + \hat{b}_2^\dagger \hat{b}_2 = \hat{a}_1^\dagger \hat{a}_1 + \hat{a}_2^\dagger \hat{a}_2, \tag{2.43}$$

the commutation relations in (2.39), (2.40) and (2.41), and a phase difference of $\pi/2$ between refleced and transmitted fields [Deg80, Zei81], we can rewrite the matrix as:

$$M_{\mathrm{BS}} = \frac{1}{\sqrt{2}} e^{i\Delta} \begin{pmatrix} ie^{i\mu} & e^{i\mu} \\ 1 & i \end{pmatrix} \tag{2.44}$$

where the factor $1/\sqrt{2}$ arises from the choice of considering a 50:50 BS. Δ is the overall phase shift and μ is the realtive phase shift. We point out that the matrix associated to a lossless BS is always unitary because of the conservation of energy (also in the classical description) and that the choice of Δ and μ depends on the physical characteristics of the device.

2.3.2 Radiation Pressure Noise

To evaluate the fluctuations in pressure we introduce the operator:

$$\hat{\mathscr{P}} \equiv 2\frac{\hbar\omega}{c}(\hat{b}_2^\dagger \hat{b}_2 - \hat{b}_1^\dagger \hat{b}_1) \tag{2.45}$$

which specifies the difference between the momenta transferred to the end mirrors of the ITF. For simplicity we assume the mass of the BS much greater than those of the end mirrors, so that we can neglect the effect of the radiation pressure on the BS. The names of the field operators that we use in the present discussion are referred to that in Fig. 2.4. We can express the last operator in terms of operators for the input modes using the BS matrix (2.44):

$$\hat{\mathscr{P}} = 2i\frac{\hbar\omega}{c}(\hat{a}_1^\dagger\hat{a}_2 + \hat{a}_2^\dagger\hat{a}_1). \tag{2.46}$$

We assume the incoming modes 1 and 2 in a coherent state and in a squeezed vacuum state respectively:

$$|\Psi\rangle = \hat{S}_2(\zeta)\hat{D}_1(\alpha)\,|0\rangle \tag{2.47}$$

we choose the phase for the mode 1 so that the amplitude α is a real number. From the properties of displacement and squeezing operators it follows that

$$\langle\hat{\mathscr{P}}\rangle_\Psi = 0 \tag{2.48}$$

$$\langle\Delta\hat{\mathscr{P}}^2\rangle_\Psi = \left(2\frac{\hbar\omega}{c}\right)^2\left[\alpha^2(\cosh^2 r + \sinh^2 r + 2\cosh r\sinh r\cos\phi) + \sinh^2 r\right] \tag{2.49}$$

If the quadrature of the sqeezed state with reduced noise is in phase with respect to the coherent excitation of mode 1, namely if $\phi/2 = 0$, (2.49) can be further simplified:

$$\langle\Delta\hat{\mathscr{P}}^2\rangle_\Psi = \left(2\frac{\hbar\omega}{c}\right)^2\left[\alpha^2 e^{2r} + \sinh^2 r\right] \tag{2.50}$$

In a measurement of duration τ[3] the fluctuation of the operator $\hat{\mathscr{P}}$ perturbs z by an amount

$$\Delta z|_{r.p.} = \frac{\tau}{2m}\sqrt{\langle\Delta\hat{\mathscr{P}}^2\rangle_\Psi} = \frac{\hbar\omega\tau}{mc}\sqrt{\alpha^2 e^{2r} + \sinh^2 r} \tag{2.51}$$

2.3.3 Shot Noise

The photon counting error is due to the fluctuations in the number operator of the mode detected by the PD (that referred to as $\hat{c}_2$ in Fig. 2.4). Once again, we have to express the output mode in terms of input modes. In doing so, we represent the effect of the propagation along the arms of the ITF through a matrix:

$$M_{\text{arms}} = e^{i\Phi}\begin{pmatrix} e^{i\varphi} & 0 \\ 0 & e^{-i\varphi} \end{pmatrix} \tag{2.52}$$

---

[3] the information about $z = z_1 - z_2$, the difference between the ITF arm lengths, is not the instantaneous value; rather it is a sort of average of z over the storage time $\tau_s = 2\mathcal{N}L/c$ the light spends in each arm. $\mathcal{N}$ is the number of bounces of the photons in a folded ITF. The best sensitivity is achieved when the measurement time τ, the time over which one averages the output to get a value for z, is near to τ_s.

where

$$\varphi = 2\frac{\omega z}{c} \tag{2.53}$$

is the phase difference between the light from the two arms, with $z = z_1 - z_2$, and

$$\Phi = 2\frac{\omega Z}{c} + \pi \tag{2.54}$$

is the mean phase, with $Z = z_1 + z_2$. The relation between input and output operators is given by[4]

$$\begin{pmatrix} \hat{c}_1 \\ \hat{c}_2 \end{pmatrix} = M_{\mathrm{BS}}^T M_{\mathrm{arms}} M_{\mathrm{BS}} \begin{pmatrix} \hat{a}_1 \\ \hat{a}_2 \end{pmatrix} = e^{i\Theta} \begin{pmatrix} -\sin(\varphi+\mu) & \cos(\varphi+\mu) \\ \cos(\varphi+\mu) & \sin(\varphi+\mu) \end{pmatrix} \begin{pmatrix} \hat{a}_1 \\ \hat{a}_2 \end{pmatrix} \tag{2.55}$$

where

$$\Theta = 2\frac{\omega Z}{c} + \mu - \frac{\pi}{2} \tag{2.56}$$

By using (2.55) we can now obtain the mean value of the number operator of the output mode:

$$\langle \hat{\mathscr{N}} \rangle_\Psi \equiv \langle \hat{c}_2^\dagger \hat{c}_2 \rangle_\Psi = \alpha^2 \cos^2(\varphi+\mu) + \sinh^2 r \sin^2(\varphi+\mu) \tag{2.57}$$

and its variance:

$$\langle \Delta \hat{\mathscr{N}}^2 \rangle_\Psi = \frac{\sin^2(2(\varphi+\mu))}{4}(\alpha^2 e^{-2r} + \sinh^2 r) \tag{2.58}$$

To evaluate how a perturbation on the photon counting affects the measure of z we need to linearize (2.57):

$$\delta\mathscr{N} = \frac{2\omega}{c}\sin(2(\varphi+\mu))(\sinh^2 r - \alpha^2)\delta z \simeq -\frac{2\omega}{c}\sin(2(\varphi+\mu))\alpha^2 \delta z; \tag{2.59}$$

by inverting (2.59) and substituting $\delta\mathscr{N}$ with the fluctuation obtained in (2.58), we find

$$\Delta z|_{s.n.} = \frac{c}{4\omega}\sqrt{\frac{1}{\alpha^2 e^{2r}} + \frac{\sinh^2 r}{\alpha^4}} \tag{2.60}$$

---

[4] M_{BS}^T is the transpose matrix of M_{BS}

2.3.4 Optimum Power

The total quantum noise on the measure of z is the quadrature sum of the two contributions (2.51) and (2.60):

$$\Delta z|_{tot} = \sqrt{\Delta z|^2_{r.p.} + \Delta z|^2_{s.n.}} = \sqrt{\left(\frac{\hbar\omega\tau}{mc}\alpha e^r\right)^2 + \left(\frac{c}{4\omega}\frac{1}{\alpha e^r}\right)^2} \tag{2.61}$$

where we have assumed that

$$\alpha^2 \gg \sinh r. \tag{2.62}$$

If we minimize the total error with respect to α^2 we find a minimum error

$$\Delta z|_{min} = \sqrt{\frac{\hbar\tau}{2m}} \tag{2.63}$$

for an optimum value of α^2:

$$\alpha^2_{opt.} = \alpha^2_0 e^{-2r} = \frac{1}{4}\frac{mc^2}{\hbar\omega}\frac{1}{\omega\tau}e^{-2r}. \tag{2.64}$$

The last equation leads to an optimum power:

$$P_{opt.} = P_0 e^{-2r} = \frac{\hbar\omega\alpha^2_0}{\tau}e^{-2r} \tag{2.65}$$

thus, if a squeezed vacuum is injected into the dark port of an ITF, the power needed to reach the optimum sensibility is reduced respect to the case in which a coherent vacuum enters the ITF. Viceversa, with the same power of the laser it is possible to reduce one of the two contributions to the quantum noise by fixing the phase of the squeezed vacuum to the laser and choosing the appropriate squeezing angle. If $\phi/2 = 0$ the vacuum is squeezed in amplitude quadrature and the radiation pressure noise is reduced, if $\phi/2 = \pi/2$ the vacuum is squeezed in phase and the shot noise is reduced.

2.4 Squeezed Light Generation

There are several way to generate squeezed light (see for instance [BR04, Ch.9]). Presently, the most robust method is based on the degenerate parametric amplification inside a nonlinear optical device [WKHW86]: the medium is pumped by a field (*pump*) at frequency $2\omega/(2\pi)$, previously generated with a Second Harmonic Generation (SHG) process [Boy03, §2.6], and a number of photons of that field is converted into pairs of photons (*signal*) with frequency $\omega/(2\pi)$ and a squeezed distibution in quadrature noise. In real experiments, the nonlinear crystal is placed inside a cavity to

enhance the efficiency of the parametric amplification, the signal to be amplified being very weak. The device is then called an Optical Parametric Oscillator (OPO).
In the next section we give a semiclassical description of how the parametric amplification acts on the signal field, following the reasoning of [Fox06, appx. B].

2.4.1 Nonlinear Optics

The propagation of electromagnetic waves through a dielectric medium is governed by the electric displacement:

$$\boldsymbol{D} = \epsilon_0 \boldsymbol{E} + \boldsymbol{P}; \tag{2.66}$$

in a nonlinear medium the polarization $\boldsymbol{P}$ depends on higher order of the electric field:

$$\boldsymbol{P} = \epsilon_0(\chi^{(1)}\boldsymbol{E} + \chi^{(2)}\boldsymbol{E}\boldsymbol{E} + \cdots) = \epsilon_0\chi^{(1)}\boldsymbol{E} + \boldsymbol{P}^{NL} \tag{2.67}$$

where the i-th-order electric susceptibility $\chi^{(i)}$ is a $(i+1)$-th-rank tensor. In the last term of (2.67) we split the polarization into its linear and nonlinear term.
Assuming a non-magnetic medium without free charges and currents, from Maxwell's equations we can derive the wave equation:

$$\left(\nabla^2 - \frac{n^2}{c^2}\frac{\partial^2}{\partial t^2}\right)\boldsymbol{E} = \frac{1}{\epsilon_0 c^2}\frac{\partial^2 \boldsymbol{P}^{NL}}{\partial t^2} \tag{2.68}$$

where $n = \sqrt{1 + \chi_{eff}^{(1)}}$ is the refractive index of the medium.
Let us now introduce a series of assumptions in order to simplify the above equation. First, we consider a fixed polarization of all the fields involved so as to substitute vectors with scalar quantities. In doing so we drop the tensor nature of the electric susceptibility and, for a fixed geometry of the crystal, we replace $\chi^{(i)}$ with its effective value $\chi_{eff}^{(i)}$, which is a scalar number. Second, we are interested only in second-order nonlinear processes, so that

$$P^{NL} = \epsilon_0 \chi_{eff}^{(2)} E^2. \tag{2.69}$$

Third, we define the direction of propagation as the z-axis. Finally, we restrict our analysis to the case where the electric field oscillates at angular frequency ω and 2ω:

$$E = \mathcal{E}_\omega(z)e^{-i(\omega t - k_\omega z)} + \mathcal{E}_{2\omega}(z)e^{-i(2\omega t - k_{2\omega} z)} + c.c. \tag{2.70}$$

where $\mathcal{E}_\omega(z)$ and $\mathcal{E}_{2\omega}(z)$ are complex amplitudes, and $k_\omega = \omega n_\omega / c$ and $k_{2\omega} = 2\omega n_{2\omega}/c$ are the wavenumbers. We point out that the refractive index depends on the frequency of the wave.

By substituting (2.70) into the simplified form of (2.68):

$$\left(\frac{\partial^2}{\partial z^2} - \frac{n^2}{c^2}\frac{\partial^2}{\partial t^2}\right) E = \frac{\chi^{(2)}_{eff}}{c^2}\frac{\partial^2 E^2}{\partial t^2} \tag{2.71}$$

and solving for the component at angular frequency ω, we obtain:

$$\left(\frac{\partial^2}{\partial z^2} - \frac{n_\omega^2}{c^2}\frac{\partial^2}{\partial t^2}\right)\left(\mathcal{E}_\omega(z)e^{-i(\omega t - k_\omega z)}\right) = \frac{\chi^{(2)}_{eff}}{c^2}\frac{\partial^2}{\partial t^2}\left(2\mathcal{E}_{2\omega}(z)e^{-i(2\omega t - k_{2\omega} z)}\mathcal{E}^*_\omega(z)e^{i(\omega t - k_\omega z)}\right). \tag{2.72}$$

After some manipulation and assuming the slowly varying envelope approximation:

$$k_\omega\left|\frac{d\mathcal{E}_\omega}{dz}\right| \gg \left|\frac{d^2\mathcal{E}_\omega}{dz^2}\right| \tag{2.73}$$

we finally obtain:

$$\frac{d\mathcal{E}_\omega(z)}{dz} = i\frac{\omega\chi^{(2)}_{eff}}{cn_\omega}\mathcal{E}_{2\omega}(z)\mathcal{E}^*_\omega(z)e^{i\Delta kz} \tag{2.74}$$

with $\Delta k = k_{2\omega} - 2k_\omega$. We cosider now a perfect phase matching condition ($\Delta k = 0$) that can be reached by using periodically-poled crystals [Boy03, §2.9] and we rewrite (2.74) as:

$$\frac{d\mathcal{E}_\omega(z)}{dz} = ig\mathcal{E}_{2\omega}(z)\mathcal{E}^*_\omega(z) \tag{2.75}$$

with the real constant g given by:

$$g = \frac{\omega\chi^{(2)}_{eff}}{cn_\omega}. \tag{2.76}$$

If the depletion of the pump field is negligible, we can rewrite its amplitude as:

$$\mathcal{E}_{2\omega} = \mathcal{E}_0 e^{i\eta} \tag{2.77}$$

with $\mathcal{E}_0$ a real number and η the phase. For a more general discussion we consider an arbitrary rotated signal field:

$$\mathcal{E}_\omega(z) \to \mathcal{E}_\omega(z)e^{-i\chi} \tag{2.78}$$

so that (2.75) becomes:

$$\frac{d\mathcal{E}_\omega(z)}{dz}e^{-i\chi} = i\gamma\mathcal{E}^*_\omega(z)e^{i(\eta+\chi)} \tag{2.79}$$

where $\gamma = g\mathcal{E}_0$. On adding and subtracting (2.79) and its complex conjugate we find:

$$\frac{d}{dz}\left(\mathcal{E}_\omega(z)e^{-i\chi} + \mathcal{E}^*_\omega(z)e^{i\chi}\right) = i\gamma\left(\mathcal{E}^*_\omega(z)e^{i(\eta+\chi)} - \mathcal{E}_\omega(z)e^{-i(\eta+\chi)}\right) \tag{2.80}$$

$$\frac{d}{dz}\left(\mathcal{E}_\omega(z)e^{-i\chi} - \mathcal{E}^*_\omega(z)e^{i\chi}\right) = i\gamma\left(\mathcal{E}^*_\omega(z)e^{i(\eta+\chi)} + \mathcal{E}_\omega(z)e^{-i(\eta+\chi)}\right). \tag{2.81}$$

In passing to a quantum description of the optical parametric amplification, we use the canonical quantization of the field and substitute $\mathcal{E}_\omega$ and $\mathcal{E}^*_\omega$ with the operators $\hat{a}$ and $\hat{a}^\dagger$ respectively. In the special case where $\eta = \pi/2$, (2.80) and (2.81) simplify to:

$$\frac{d}{dz}\left(\hat{a}(z)e^{-i\chi} + \hat{a}^\dagger(z)e^{i\chi}\right) = -\gamma\left(\hat{a}^\dagger(z)e^{i\chi} + \hat{a}(z)e^{-i\chi}\right) \tag{2.82}$$

$$\frac{d}{dz}\left(\hat{a}(z)e^{-i\chi} - \hat{a}^\dagger(z)e^{i\chi}\right) = \gamma\left(-\hat{a}^\dagger(z)e^{i\chi} + \hat{a}(z)e^{-i\chi}\right) \tag{2.83}$$

where we recognize the rotated quadrature operators (2.7) and (2.8). Thus:

$$\frac{d}{dz}\hat{X}_\chi(z) = -\gamma\hat{X}_\chi(z) \tag{2.84}$$

$$\frac{d}{dz}\hat{Y}_\chi(z) = \gamma\hat{Y}_\chi(z) \tag{2.85}$$

which solutions are exponential functions:

$$\hat{X}_\chi(z) = \hat{X}_\chi(0)e^{-\gamma z} \tag{2.86}$$

$$\hat{Y}_\chi(z) = \hat{Y}_\chi(0)e^{\gamma z}. \tag{2.87}$$

If the signal field to be amplified is the vacuum state, then only the fluctuations of the quadrature operators enter the above equations, since $\langle\hat{X}_\chi\rangle_\zeta = \langle\hat{Y}_\chi\rangle_\zeta = 0$. The result is that, passing through the nonlinear medium, fluctuations in the rotated amplitude quadrature operator $\hat{X}_\chi(z)$ are reduced while fluctuations in the rotated phase quadrature operator $\hat{Y}_\chi(z)$ are increased: we have just described an amplitude squeezing. If we had chosen $\eta = -\pi/2$, we would have achieved a phase squeezing.

2.5 Squeezed Light Detection

To properly characterize a squeezed state we need to obtain informations about the quantum noise in different field quadratures, this is done through the use of the *Balanced Homodyne Detector* [YC83], a device composed by two photodiodes (PDs) and a 50:50 BS.

Before describe how the homodyne works, we introduce a trick to better handle the mathematical calculation. In quantum optics it is often useful to linearize the field operators by decomposing them in two parts: a complex number that represents the steady amplitude (i.e. the mean value of the operator) and an operator that represents the quantum fluctuation. For instance we can rewrite the annihilation operator as

$$\hat{a} = \alpha + \delta\hat{a} \tag{2.88}$$

with

$$\langle \delta\hat{a} \rangle = 0. \tag{2.89}$$

If we now calculate the linearized photon number from (2.88), we find:

$$\hat{N} = \hat{a}^\dagger \hat{a} = |\alpha|^2 + \alpha^* \delta\hat{a} + \alpha\delta\hat{a}^\dagger + \delta\hat{a}^\dagger \delta\hat{a} \simeq |\alpha|^2 + \alpha(\delta\hat{a} + \delta\hat{a}^\dagger) \tag{2.90}$$

where in the last term we have considered α as a real number and we have neglected higher order fluctuations[5]. By considering (2.4) and (2.18) we can give to the last equation the simple form:

$$\hat{N} = \bar{N} + 2\alpha\delta\hat{X} \tag{2.91}$$

which leads to an important result: the fluctuation in photon number depends only on the fluctuation in amplitude quadrature operator. If we then use only one PD to detect a particular state of light, we can detect only fluctuation in one quadrature. That is why we need two PDs to fully characterize a squeezed state.

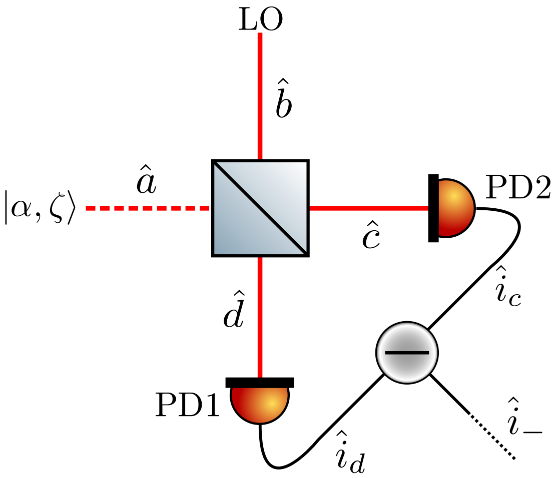

FIGURE 2.6: Scheme of the balanced homodyne detector

The basic setup for a balanced homodyne detector is illustrated in Fig. 2.6. The beams that enter the BS are the squeezed state[6], associated with the linearized operator (2.88), and the so-called *Local Oscillator* (LO) which has the same frequency of the other field

---

[5] this assumption is realistic for bright coherent state, where $\langle \hat{a} \rangle \gg \sqrt{\langle \Delta\hat{a}^2 \rangle}$. For weak field, higher order fluctuations are to be considered and for the special case of a vacuum state the constant term in (2.88) is zero and the linearized operator becomes $\hat{a} = \delta\hat{a}$

[6] not necessarily the squeezed vacuum, a squeezed bright state $|\alpha, \zeta\rangle$ can be obtained by applying the displacement operator to the squeezed vacuum: $|\alpha, \zeta\rangle = \hat{D}(\alpha)\hat{S}(\zeta)\,|0\rangle$

and is described by

$$\hat{b} = e^{i\Phi}(\beta + \delta\hat{b}) \tag{2.92}$$

where Φ is the phase difference between the two input fields. We choose the phases of the incoming beams so that α and β are real numbers and, applying the BS matrix (2.44), we can express the transformation acting on the operators as:

$$\hat{c} = \frac{e^{i(\Delta+\mu)}}{\sqrt{2}}(i\hat{a} + \hat{b}) \tag{2.93}$$

$$\hat{d} = \frac{e^{i\Delta}}{\sqrt{2}}(\hat{a} + i\hat{b}). \tag{2.94}$$

The operators related to the photo-currents are given by:

$$\hat{i}_c \propto \hat{c}^\dagger\hat{c} = \frac{1}{2}(\hat{a}^\dagger\hat{a} - i\hat{a}^\dagger\hat{b} + i\hat{a}\hat{b}^\dagger + \hat{b}^\dagger\hat{b}) \tag{2.95}$$

$$\hat{i}_d \propto \hat{d}^\dagger\hat{d} = \frac{1}{2}(\hat{a}^\dagger\hat{a} + i\hat{a}^\dagger\hat{b} - i\hat{a}\hat{b}^\dagger + \hat{b}^\dagger\hat{b}) \tag{2.96}$$

and, substituting the operators with the linearized form, the difference photo-current is

$$\begin{aligned} \hat{i}_- &= \hat{i}_c - \hat{i}_d \propto i(\hat{a}^\dagger\hat{b} + \hat{a}\hat{b}^\dagger) && (2.97) \\ &= i[2\alpha\beta\cos\Phi + 2\alpha\delta\hat{X}^b_{-\Phi} + 2\beta\delta\hat{X}^a_\Phi + \mathcal{O}(\delta^2)] && (2.98) \end{aligned}$$

where $\mathcal{O}(\delta^2)$ contains all higher-order fluctuation terms and, from (2.7):

$$\delta\hat{X}^a_\Phi = \frac{1}{2}(\delta\hat{a}e^{-i\Phi} + \delta\hat{a}^\dagger e^{i\Phi}) \tag{2.99}$$

$$\delta\hat{X}^b_{-\Phi} = \frac{1}{2}(\delta\hat{b}e^{i\Phi} + \delta\hat{b}^\dagger e^{-i\Phi}). \tag{2.100}$$

In the interesting case where the squeezed state is a vacuum state:

$$\alpha = \langle\hat{a}\rangle_\zeta = 0, \tag{2.101}$$

we can rewrite (2.97) as:

$$\hat{i}_- \propto 2\beta\delta\hat{X}^a_\Phi \tag{2.102}$$

Thus, the fluctuations of the squeezed state in the quadrature $\hat{X}^a_\Phi$ are amplified by the amplitude of the LO, while the LO noise is suppressed. Equation (2.102) allows us to measure the fluctuation of any quadrature of the squeezed field by changing the phase difference between the two input fields, for instance by change the optical path of one beam.

Chapter 3

Coherent Control Loop

The quantum noise suppression described in the previous chapter is efficient only if the phase of the squeezed field is kept fixed with respect to the phase of the main field circulating in the ITF. Fluctuations of the squeezed ellipse, as well as optical losses, decrease the effective squeezing level (see §3.2.1). These fluctuations happen because mechanical noises change the optical path of the radiation field in a random fashion. A signal which encodes the phase difference between the two fields must be obtained to correct the squeezing angle, but the squeezed vacuum itself is too weak to obtain such an error signal. Valbruch *et al.* [VCH+06] proposed to introduce a second field, called *Quadrature Control Field* (QCF), which carries information on the squeezing angle and can be used instead of the squeezed vacuum to do the work. The QCF is injected into the OPO cavity, senses the nonlinearity of the medium and the information carried by it outside the cavity is used to generate two error signals. The first error signal is used to control the relative phase between the QCF and the OPO pump field; the second one is used to control the relative phase between the QCF and LO of the homodyne detector. The homodyne is used in a preliminary procedure before the injection of the squeezed vacuum in the ITF in order to measure the squeezing level produced in the OPO. The control network that meets these goals was called *Coherent Control Loop*.

3.1 Quadrature Control Field

When the QCF, at frequency $(\omega + \Omega)/(2\pi)$, enters the OPO cavity, it interacts with the pump field at frequency $2\omega/(2\pi)$ and converts a number of photons of the pump in pairs of photons at frequency $(\omega + \Omega)/(2\pi)$ (signal) and $(\omega - \Omega)/(2\pi)$ (idler) via the parametric amplification [Boy03, §2.5].

Before the nonlinear interaction, the expectation values of the annihilation operators for the signal and the idler fields are respectively:

$$\langle \hat{a}_+ \rangle_{QCF} \equiv \langle \hat{a}(\omega+\Omega) \rangle_{QCF} = \alpha_\Omega \tag{3.1}$$

$$\langle \hat{a}_- \rangle_{QCF} \equiv \langle \hat{a}(\omega-\Omega) \rangle_{QCF} = 0 \tag{3.2}$$

where α_Ω is chosen to be real, for simplicity.
Following the formalism of [CS85] we introduce the two-mode quadrature operators[1]:

$$\hat{a}_1(\Omega) = \left(\frac{\omega+\Omega}{2\Omega}\right)^{1/2} \hat{a}_+ + \left(\frac{\omega-\Omega}{2\Omega}\right)^{1/2} \hat{a}_-^\dagger \simeq \frac{1}{\sqrt{2}}\left(\hat{a}_+ + \hat{a}_-^\dagger\right) \tag{3.3}$$

$$\hat{a}_2(\Omega) = -i\left(\frac{\omega+\Omega}{2\Omega}\right)^{1/2} \hat{a}_+ + i\left(\frac{\omega-\Omega}{2\Omega}\right)^{1/2} \hat{a}_-^\dagger \simeq \frac{1}{\sqrt{2}}\left(-i\hat{a}_+ + i\hat{a}_-^\dagger\right) \tag{3.4}$$

and the two-mode squeezing operator:

$$\hat{S}(r,\phi) = \exp\left[r\left(\hat{a}_+\hat{a}_- e^{-i\phi} - \hat{a}_+^\dagger \hat{a}_-^\dagger e^{i\phi}\right)\right] \tag{3.5}$$

with squeezing factor r and squeezing angle ϕ. From the Baker-Hausdorff lemma [Mer70, (8.105)] the following useful relations can be derived:

$$\hat{S}(r,\phi)\hat{a}_\pm \hat{S}^\dagger(r,\phi) = \hat{a}_\pm \cosh r + \hat{a}_\mp^\dagger e^{i\phi} \sinh r \tag{3.6}$$

$$\hat{S}(r,\phi)\hat{a}_\pm^\dagger \hat{S}^\dagger(r,\phi) = \hat{a}_\pm^\dagger \cosh r + \hat{a}_\mp e^{-i\phi} \sinh r. \tag{3.7}$$

After the parametric amplification, the quadrature operators become:

$$\begin{pmatrix} \hat{b}_1(\Omega) \\ \hat{b}_2(\Omega) \end{pmatrix} = \hat{S}(r,\phi) \begin{pmatrix} \hat{a}_1(\Omega) \\ \hat{a}_2(\Omega) \end{pmatrix} \hat{S}^\dagger(r,\phi) \tag{3.8}$$

$$= \begin{pmatrix} \cosh r + \sinh r \cos\phi & \sinh r \sin\phi \\ \sinh r \sin\phi & \cosh r - \sinh r \cos\phi \end{pmatrix} \begin{pmatrix} \hat{a}_1(\Omega) \\ \hat{a}_2(\Omega) \end{pmatrix} \tag{3.9}$$

and their expectation values take the form:

$$\langle \hat{b}_1(\Omega) \rangle_{QCF} = \frac{\alpha_\Omega}{\sqrt{2}}[(\cosh r + \sinh r \cos\phi) - i \sinh r \sin\phi] \tag{3.10}$$

$$\langle \hat{b}_2(\Omega) \rangle_{QCF} = \frac{\alpha_\Omega}{\sqrt{2}}[\sinh r \sin\phi - i(\cosh r - \sinh r \cos\phi)]. \tag{3.11}$$

---

[1] To justify the following simplified expressions we remember that in realistic experiments $\omega/(2\pi)$ is of the order of 100THz while $\Omega/(2\pi)$ is usually of the order of 10MHz

To derive the corresponding electrical field we must move on to the time domain with a Fourier transformation:

$$\hat{b}_m(t) = \hat{b}_m(\Omega)e^{-i\Omega t} + \hat{b}_m^{\dagger}(\Omega)e^{i\Omega t}, \qquad m = 1, 2. \tag{3.12}$$

By replacing the above results into the expression

$$\hat{E}(t) \propto \hat{b}_+(t) + \hat{b}_-(t) \tag{3.13}$$

with

$$\hat{b}_\pm(t) = \frac{1}{2}\left(\hat{b}_1(t) \pm i\hat{b}_2(t)\right) e^{\mp i\omega t}, \tag{3.14}$$

we obtain the outgoing QCF:

$$\langle\hat{E}(t)\rangle_{QCF} \propto \frac{1+g}{\sqrt{2g}}\alpha_\Omega \cos((\omega+\Omega)t) - \frac{1-g}{\sqrt{2g}}\alpha_\Omega \cos((\omega-\Omega)t-\phi) \tag{3.15}$$

where $g = \exp(2r)$.

Equation (3.15) is the desired result: the QCF oscillates at two frequencies, equally separated by the carrier frequency $\omega/(2\pi)$, and it embodies information about the squeezing angle ϕ. In the following two sections we will see how to obtain the error signals from this field. The advantage of this method is that no bright field of the squeezed beam is required, so no technical noiseis is added to the squeezed vacuum beam.

3.1.1 Phase Control of the Pump Field

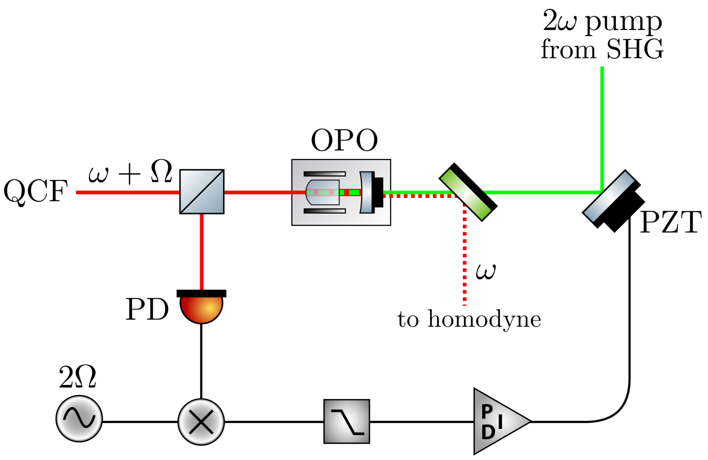

FIGURE 3.1: Schematic control loop for the locking of the pump angle

To obtain the error signal for the loop that locks the pump field phase to that of the QCF, we detect the QCF with a single PD placed outside the OPO. The photocurrent of the PD is proportional to the square of the incident field:

$$I_{QCF} \propto \langle \hat{E}(t) \rangle^2_{QCF} \tag{3.16}$$

and it is composed by components with different frequencies. Demodulating this signal at frequency $2\Omega/(2\pi)$, namely mixing it with a signal at frequency $2\Omega/(2\pi)$ and low-pass filtering it, provides the error signal

$$S^{pump}_{err} \propto \frac{(g^2-1)\alpha^2_\Omega \sin\phi}{4g} \tag{3.17}$$

which depends on the squeezing angle, i.e. the phase difference between the squeezed vacuum and the pump. This signal is fed to a piezoelectric (PZT) actuator which hosts a mirror (see Fig. 3.1) in order to change the optical path of the pump field and hence to lock its phase (and that of the squeezed vacuum) with respect to the phase of the QCF.

3.1.2 Phase Control of the LO

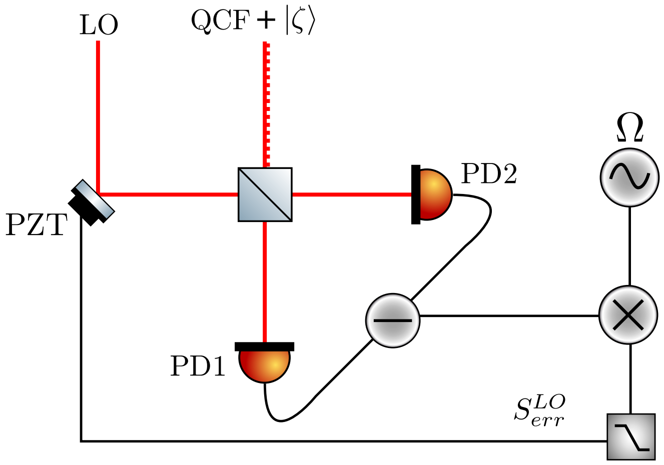

Figure 3.2: Schematic control loop for the locking of the LO angle

A certain amount of the QCF is transmitted through the OPO and enters the homodyne detector together with the squeezed vacuum. Let describe the LO entering the BS of the homodyne with the complex notation:

$$E_{LO}(t) \propto \alpha_{LO} e^{-i(\omega t+\varphi)}. \tag{3.18}$$

with α_{LO} a real number. The fields at the two PDs of the homodyne are found using the BS matrix (2.44); we can then calculate the difference current:

$$i_-(t) \propto |E_{PD1}(t)|^2 - |E_{PD2}(t)|^2 \tag{3.19}$$

$$\propto \frac{\alpha_{LO}\alpha_\Omega}{\sqrt{2g}}\left[(1+g)\sin(\Omega t-\varphi)+(1-g)\sin(\Omega t+\varphi+\phi)+(2\omega\, terms)\right]. \tag{3.20}$$

The 2ω terms are too fast for the PD and are averaged out, resulting in a DC offset. Finally, the signal is demodulated by mixing it with the signal $\alpha_d\cos(\Omega t+\chi)$ and low-pass filtered. The result is the error signal:

$$S_{err}^{LO} \propto \frac{\alpha_d\alpha_{LO}\alpha_\Omega}{2\sqrt{2g}}\left[-(1+g)\sin(\varphi+\chi)+(1-g)\sin(\varphi+\phi-\chi)\right]. \tag{3.21}$$

By choosing the demodulation signal phase so that $\chi=-\varphi$, the last expression assumes the simple form:

$$S_{err}^{LO} \propto \frac{\alpha_d\alpha_{LO}\alpha_\Omega(1-g)}{2\sqrt{2g}}\sin(2\varphi+\phi), \tag{3.22}$$

After the squeezing angle *phi* is stabilized using the completely independent pump path control loop, the homodyne error signal depends merely on φ and thereby can be directly employed to stabilize the homodyne detection angle acting on a phase shifter (like a PZT-mounted mirror) placed in the optical path of the LO (see Fig3.2). Once the phase difference between the LO and the squeezed vacuum is stabilized, it is possible to measure the variance of any quadrature of the squeezed field (see §2.5). From this measure one obtains the squeezing level produced in the OPO.

3.2 Phase Control in Advanced Virgo

So far the technique to lock the QCF to other fields circulating on the squeezer bench was described, what remains to do is to extract the information on the phase difference between the squeezed vacuum and the ITF carrier in the detection bench. The error signal for the phase control is derived using the detected light transmitted through one the output mode-cleaners where the squeezing coherent control sidebands beat with the spatially filtered carrier light. The beat note is then demodulated at Ω in the same way explained in 3.1.2. This signal is fed to a phase shifter which corrects the phase of the master laser upstream as explained in the next chapter. This control system, which will be implemented on Virgo squeezer bench, differs from the usual method where the error signal corrects the optical path of the squeezed vacuum with a PZT-mounted mirror. The principal benefit of this method is that the squeezed vacuum does not sense scattering on the moving mirror and so stray light issues are reduced.

3.2.1 Squeezing Degradation and Targets

When a squeezed state experiences optical losses, it remains squeezed but the squeeze factor is reduced because optical losses correspond to mixing the state with the coherent vacuum state. Let ϵ be the relative power loss, $\langle\Delta\hat{X}_{\chi}^{2}\rangle_{\zeta}$ the variance of the generic quadrature operator of the squeezed state (see 2.30) and $\langle\Delta\hat{X}_{vac}^{2}\rangle$ the quadrature variance of the coherent vacuum state; than the resulting quadrature variance reads [Che07, §2.9.4]

$$\langle\Delta\hat{X}_{\chi}^{2}\rangle_{\zeta}' = (1-\epsilon)\langle\Delta\hat{X}_{\chi}^{2}\rangle_{\zeta} + \epsilon\langle\Delta\hat{X}_{vac}^{2}\rangle \tag{3.23}$$

Note that the quantity ϵ in the above calculation includes many contributions, like propagation losses due to non perfect optics, quantum efficiency of the photodiodes, mode mismatch and clipping of the beams.

Also fluctuations of the squeezing ellipse angle deteriorate the final squeezing level by mixing the squeezed and anti-squeezed quadratures, in the approximation of small angle fluctuations this degradation can be described by [ZGC⁺03]:

$$\langle\Delta\hat{X}_{\phi/2}^{2}\rangle_{\zeta}' = \langle\Delta\hat{X}_{\phi/2}^{2}\rangle_{\zeta}\cos^{2}\theta_{RMS} + \langle\Delta\hat{Y}_{\phi/2}^{2}\rangle_{\zeta}\sin^{2}\theta_{RMS} \tag{3.24}$$

where $\langle\Delta\hat{X}_{\phi/2}^{2}\rangle_{\zeta}$ is the variance of the squeezed quadrature, $\langle\Delta\hat{Y}_{\phi/2}^{2}\rangle_{\zeta}$ the variance of the anti-squeezed quadrature and θ_{RMS} is the RMS value of phase fluctuations. Fig. 3.3 shows the combined effect of optical losses and ellipse fluctuations on the squeezing level.

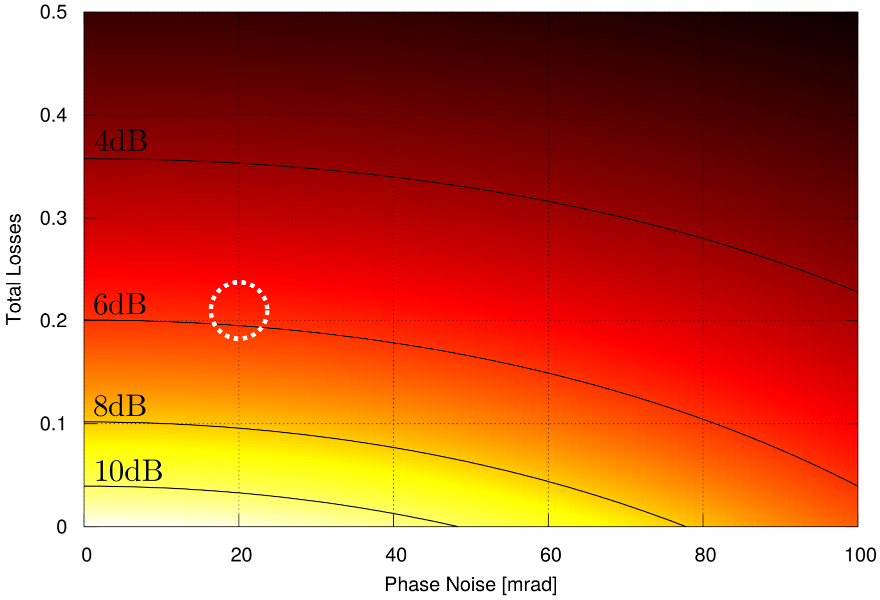

FIGURE 3.3: Contour plot of the final squeezing level as a function of squeezing angle fluctuations and optical losses, the initial squeezing level is $12dB$

The target for the Advanced Virgo (AdV) squeezed light source is to produce $12dB$ of frequency independent squeezing from the OPO across the $10Hz$ to $10kHz$ detection band. Considering that the expected overall losses are 22%, a target of a maximum of $20mrad$ rms of squeezing ellipse phase noise at the readout PD is set if $6dB$ of squeezing enhancement at the ITF are required. The dotted circle in Fig. 3.3 represent the actual target.

3.2.2 Optical Setup

Figure 3.4 illustrates the simplified optical setup of Virgo experiment, including the ITF (not in scale!), the squeezer bench and the detection bench. A pick-off from the ITF laser beam is send to the squeezer bench via a $50m$ optical fiber, after being frequency-shifted by $\Omega_{AOM}/(2\pi) = 80MHz$ with an acousto-optic modulator (AOM); in this way the loop operates at a frequency well above the Flicker noise dominated region. Than PLL1, operating at $80MHz$, is used to lock the main laser of the squeezer bench to that of the ITF laser, restoring the original frequency. The main laser beam is used to generate the pump field at the SHG cavity; the pump field, in turn, is injected into the OPO cavity where the squeezed vacuum is generated via the parametric amplification (see §2.4). PLL2 is used to lock the control laser (which generates the QCF) to the main laser with a frequency shift of $\Omega_{CC}/(2\pi) = 7MHz$; this value is close to half of the free spectral range of the signal recycling cavity [Mee88] because the control beam sidebands must be totally reflected when they are injected into the dark port of the ITF with the squeezed light.

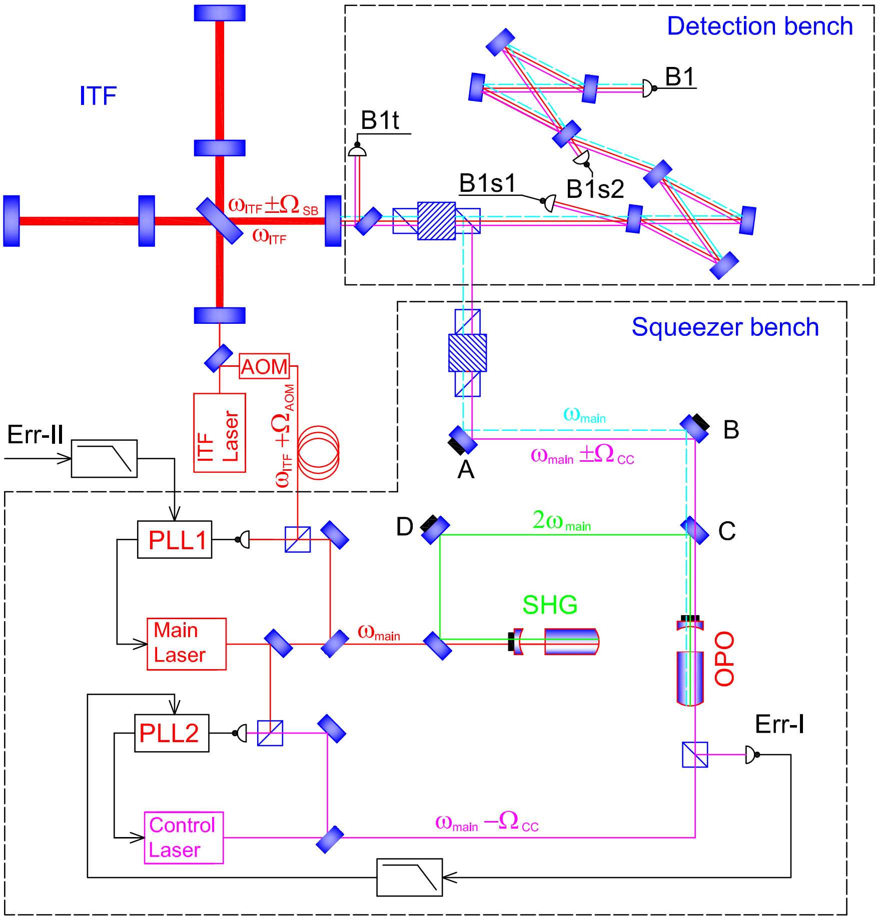

FIGURE 3.4: Schematic of the Coherent Control system for AdV. Red line: ITF and main laser beam, Green line: second harmonic beam, Purple: QCF, Cyan: squeezed light. Courtesy of the Advanced Virgo Squeezing Working Group

Chapter 4

Experimental Setup

In this chapter we are going to describe how we implemented the optical bench for the study of our nested loop system. The first section explains what an OPLL is and how can be realized. The second section focuses on the optical bench. In the last section the experimental results are presented.

4.1 Optical Phase Locked Loop

In §3.1 we have stated that the QCF must be frequency-shifted against the fundamental frequency $\omega/(2\pi)$. To experimentally prepare such a field, we use another laser (*slave*), which is frequency locked to the main laser (*master*) with a fixed difference of frequency between them. In this section we are going to introduce the opto-electronic configuration that enables us to reach this goal, called *optical phase locked loop* (OPLL).
The first step of this technique consists in overlapping a pick-off of the two laser beams via a 50:50 BS (see Fig. 4.1), then the outgoing field (the sum of the input fields) is fed to a PD which produces a current proportional to the power of the incoming light, i.e. quadratic in the input field. This photocurrent would be composed by two components which oscillates at the sum and at the difference of the frequency of the two lasers, but the fast component is averaged out by the PD; therefore the outcoming signal is a sinusoidal signal oscillating at the difference in frequency between the two lasers with a DC offset which is removed with a capacitor in series with the PD output. To maximize the beat note amplitude the two beams must have the same beam waist dimension and position, their wavevectors must be parallel and the polarizations must be the same. This signal is fed to one of the inputs of a device called *phase frequency detector* (PFD), the other input, the reference signal, is a sinusoidal signal oscillating at frequency $\Omega/(2\pi)$. The output signal is proportional to the phase difference between

the beat note and the reference oscillator. Using a low pass filter the loop can be closed by feeding the slave laser's fast input with this error signal. The fast input controls a PZT that can change the length of the laser cavity and hence the frequency of the outgoing radiation field.

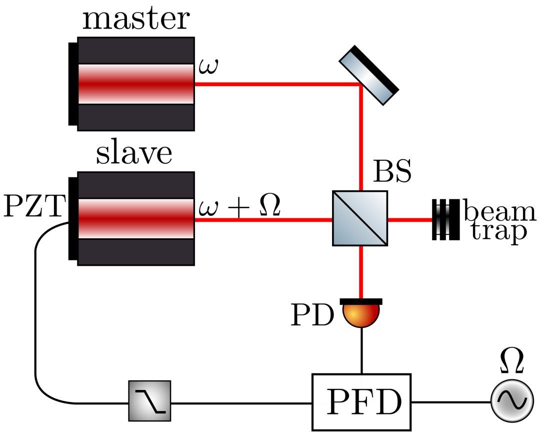

FIGURE 4.1: Basic setup for an OPLL

The control system shown above is an adjustment to the more general PLL, a negative feedback control system widely employed to generate a signal with a fixed phase difference with respect to an input periodic signal. The simplest PLL diagram is depicted in Fig. 4.2 with the essential blocks: a phase detector, a loop filter and a voltage-controlled oscillator (VCO). The input is a reference harmonic signal with

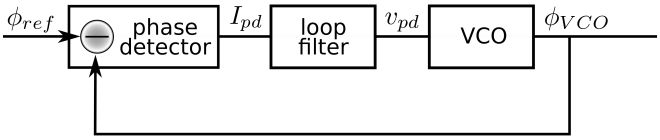

FIGURE 4.2: Block diagram of a PLL

phase $\phi_{ref}(t) = \omega_{ref} \cdot t + \phi_{0,ref}$ which enters the phase detector along with the signal outgoing from the VCO, with phase $\phi_{VCO}(t) = \omega_{VCO}(t) \cdot t + \phi_{0,VCO}(t)$. The phase detector output, i.e. the error signal of the loop, is proportional to the difference between the two phases:

$$I_{pd}(t) = K_{pd} \left(\phi_{ref}(t) - \phi_{VCO}(t) \right) \tag{4.1}$$

where K_{pd} is a constant with unit of measurement given in A/rad. After going through the loop filter, which is essentially a low-pass filter and a current-to-voltage converter, the signal $v_{pd}(t)$ is fed to the VCO. This last block produces a periodic signal with instantaneous frequency proportional to the input voltage:

$$\omega_{VCO}(t) = \omega_0 + K_{VCO} \cdot v_{pd}(t) \tag{4.2}$$

where K_{VCO} is a constant expressed in Hz/V and $\omega_0/(2\pi)$ is the central frequency of the VCO; because the frequency is the time derivative of the phase, the last equation can be written as:

$$\frac{d\phi_{VCO}(t)}{dt} = K_{VCO} \cdot v_{pd}(t). \tag{4.3}$$

It is worth noting that in the OPLL the VCO consists of the set of the two lasers, the BS and the PD: the output of the loop is the beat note and not the frequency of the slave laser.

4.1.1 Phase Frequency Detector

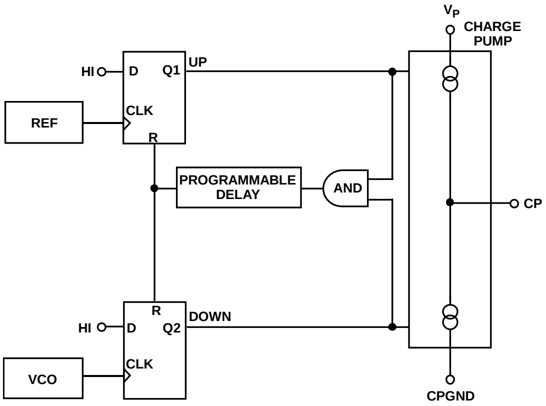

FIGURE 4.3: schematic of a PFD

Among different phase detectors (mixer phase detector, XOR phase detector...), the PFD is used to implement a digital PLL (hereinafter the LOW state and the HIGH state of digital signals will be called 0 and 1 respectively). It consists of two D-type flip-flops as shown in Fig. 4.3. The outputs of the flip-flops control two current sources, called *charge pump* (CP), which can increase or decrease the charge collected on the plates of a capacitor in series with the PFD[1].

A D-type flip-flop is a circuit that can be used as a delay line to store digital input information. It has four input channels: data D, clock CLK, set S and reset R. When S and R are set to 0, the output channel Q follows the data with some delay because it can change its value at the selected edge of the clock signal, as shown in Fig. 4.4. When R is set to 1 and S is 0, the output is forced to 0 independently from D and CLK inputs.

The inputs of the PFD (the reference signal and the beat note from the PD in the case of an OPLL) are fed to the CLK channels of the two flip-flops, the S channel of both of them is set to 0 and the D channel is set to 1. The output channels Q1 and Q2 enable the UP and DOWN source respectively when in state 1. If they are turned to

---

[1] the capacitor(s) belonging to the loop filter

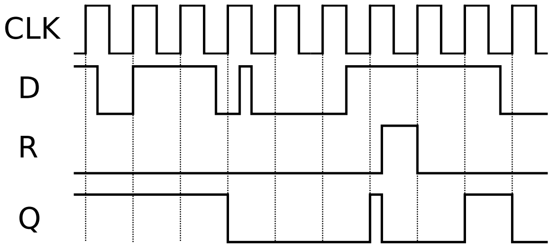

Figure 4.4: behavior of a D-type flip-flop triggered on the rising edge of the clock and with S=0

1 simultaneously, a feedback network composed by an AND gate and a programmable delay line ensures the reset of both flip-flops after a small delay of time.

Let us consider now two important cases of how a PFD works. First, we assume that the signal $v_{ref}(t)$ has a frequency higher than that of $v_{VCO}(t)$, as shown in Fig. 4.5. In this case the UP current source is enabled most of the time: Q1 takes on value 1 after the first rising edge of the reference signal and returns to 0 as soon as the PFD detects a rising edge of the VCO signal; being the rising edges of $v_{VCO}(t)$ less frequent than those of $v_{ref}(t)$, the charge pump erogates positive current most of the time so that the voltage collected in the loop filter capacitor forces the VCO to increase the frequency of its output. The second configuration happens when the input signals have equal frequencies but a difference in phase, as shown in Fig. 4.6; the output of the CP is a series of postive current pulses that ensures the phase alignment of the VCO with the reference signal. If we had the opposite condition, i.e. $\omega_{ref} < \omega_{VCO}$ for the first case and $\phi_{0,ref} < \phi_{0,VCO}$ for the second case, we would find negative values for the current from the CP.

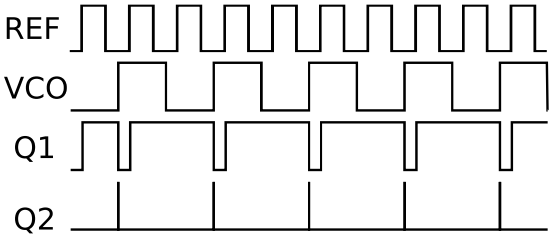

Figure 4.5: behavior of a PFD when $\omega_{ref} > \omega_{VCO}$

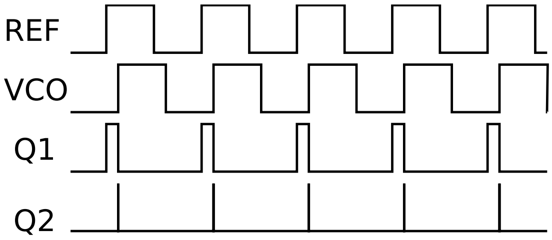

Figure 4.6: behavior of a PFD when $\omega_{ref} = \omega_{VCO}$ and $\phi_{0,ref} > \phi_{0,VCO}$

4.1.2 Transfer Functions

To obtain the closed-loop transfer function (CLTF), we have to specify the frequency response of any block of the loop [Gar05, §2.1]. In order to use the Laplace transform we must consider a linear model of the system by assuming the two lasers closed to the lock condition. This implies that the central frequency of the VCO can be set equal to that of the reference signal. The effect of the PFD is independent of the frequency of the input signal, thus its transfer function is:

$$H_{pd}(s) = K_{pd} = \frac{I_{CP}}{2\pi} \tag{4.4}$$

where I_{CP} is the current generated by the CP while activated. The loop filter is

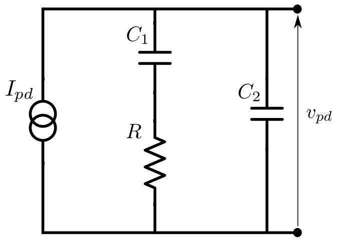

FIGURE 4.7: Loop filter layout

a second order low-pass filter with a current signal in input and a voltage signal in output, as shown in Fig. 4.7. The transfer function is given by $F(s) = v_{pd}(s)/I_{pd}(s)$, therefore it is the equivalent impedence in the frequency domain:

$$F(s) = (Z_{C_1} + R) \parallel Z_{C_2} = \frac{1 + sRC_1}{s^2RC_1C_2 + s(C_1 + C_2)} \tag{4.5}$$

where $Z_C = 1/sC$. The loop filter used in this work was chosen in order to have a loop bandwidth of $50kHz$ and a phase margin of $\sim 45°$; the software ADIsimPLL [Ana] developed by Analog Devices suggested the values presented in Table 4.1 for the loop components. Finally, by taking the Laplace transform of 4.3, we obtain:

$$s\phi_{VCO}(s) = K_{VCO} \cdot v_{pd}(s) \tag{4.6}$$

hence, the phase transfer function of the last block is:

$$H_{VCO}(s) = \frac{K_{VCO}}{s} \tag{4.7}$$

which is an integration in the time domain. For an OPLL K_{VCO} is the PZT tuning coefficient of the laser, in the present work $K_{VCO} = 2MHz/V$ (see §4.2).

We can represent a generic negative feedback network (see Fig. 4.8) with its forward

$$\begin{aligned} C_1 &= 22nF \\ C_2 &= 100nF \\ R &= 75\Omega \end{aligned}$$

TABLE 4.1: values of the loop filter components

transfer function $A(s)$ and its feedback transfer function $B(s)$; the CLTF is defined as:

$$H(s) = \frac{A(s)}{1 + A(s)B(s)}, \tag{4.8}$$

where $A(s)B(s)$ is open-loop transfer function (OLTF). The PLL OLTF is the product of the three-block transfer functions:

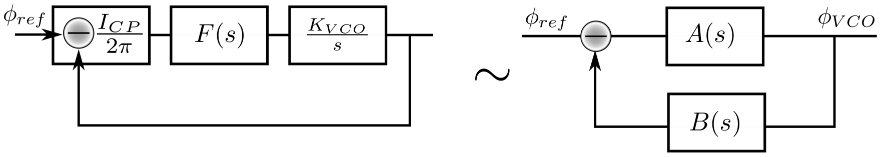

FIGURE 4.8: comparison between the PLL and a generic feedback loop

$$H_{OL}(s) = K_{pd}F(s)\frac{K_{VCO}}{s} \tag{4.9}$$

while the feedback transfer function is the identity transformation (sometimes the feedback line can host a frequency divider, which divides the frequency of its input signal by a factor N so that its transfer function can be expressed as $H_{div} = 1/N$). Finally, the CLTF function for the PLL is given by:

$$H(s) = \frac{\phi_{VCO}(s)}{\phi_{ref}(s)} = \frac{K_{VCO}K_{pd}F(s)}{s + K_{VCO}K_{pd}F(s)}. \tag{4.10}$$

In figure 4.9 are shown the Bode plots of the OLTF and CLTF of the PLL with the loop filter components of table 4.1 and with the charge pump current set to its maximum value $I_{CP} = 2.55mA$ (see next section).

4.1.3 PLL Board

The slave laser (Mephisto of Coherent [Coh]) has a PZT tuning coefficient of $2MHz/V$ and the correction signal from the PFD has values from $0V$ to $5V$. On the other hand, the frequency drift of lasers in the room where this thesis was developed reached maximum values of $180MHz/h$ due to temperature variation between night and day. It is clear that the action of the PZT alone is not sufficient to ensure long term stability

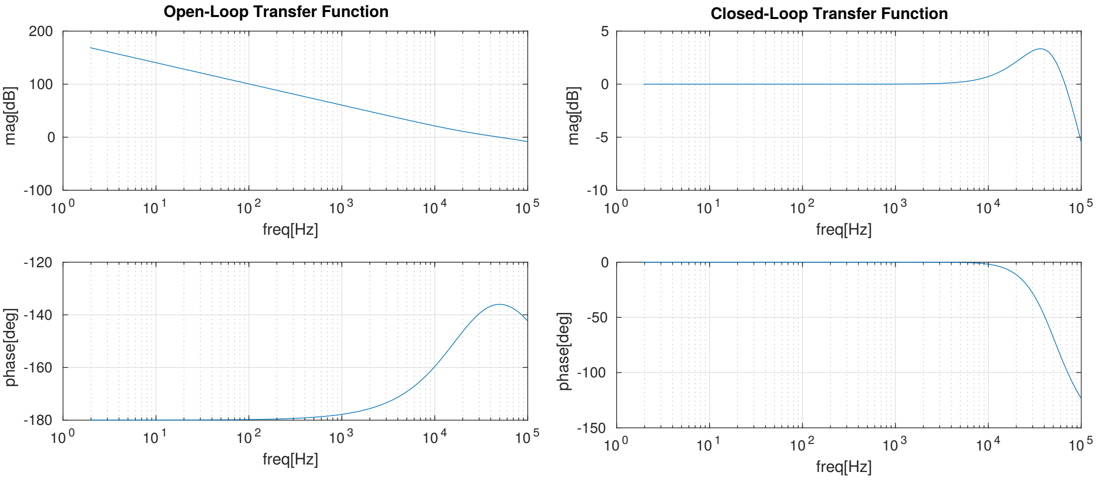

FIGURE 4.9: Bode plots of the PLL transfer functions

of the PLL, thus another servo loop has been implemented to control the temperature of the laser's crystal, the thermal tuning coefficient of the Mephisto being about $-3GHz/V$. The control system on the PZT of the laser is faster than that acting on the Peltier cell to control the temperature ($50kHz$ of bandwidth against $\sim 1Hz$), that is why the former is called FAST loop and the latter SLOW loop. A board has

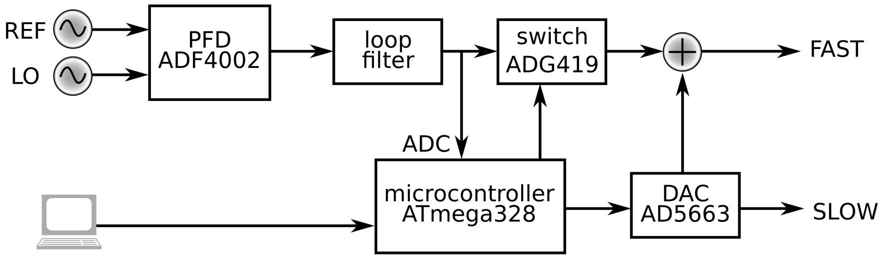

FIGURE 4.10: Block dagram of the PLL board

been developed to implement both loops and to manage the communication with an external PC through the serial protocol. In Appx. A are shown the circuit diagrams of the board. A block diagram is shown in Fig. 4.10; the core of the board is an 8-bit microcontroller (μC) unit (ATmega328 of Atmel). The PFD used is ADF4002 of Analog Devices [Ana15], which has the following main features:

- detects signals with power from $-10dBm$ to $0dBm$ and frequency between $5MHz$ and $400MHz$;
- the CP current can be set in 8 steps: $I_{CP} = I_{CP,max} \cdot j/8$, with $j = 1, \ldots, 8$. $I_{CP,max} = 25.5/R_{set}[A]$ (see datasheet), the resistor mounted on the board ($R7$ in Fig. A.1) was $R_{set} = 10k\Omega$ so that $I_{CP,max} = 2.55mA$;
- has a 24-bit input shift register for the SPI communication which controls four latches: an N counter, an R counter, an initialization latch and a function latch;

- the 13-bit N counter and the 14-bit R counter control two frequency dividers which enable to lock the VCO at a frequency f_{VCO} related to the reference frequency f_{ref} by $f_{VCO} = f_{ref} \cdot N/R$;
- the initialization and the function latches set the polarity of the PFD, set the CP current and control the multiplexer output (MUXOUT in Fig. A.1), which allows the user to access various internal points on the chip. It could set as a digital lock detect, i.e. the multiplexer output is set high when the phase error on three consecutive phase detector cycles is less than $15ns$ and is set low otherwise (see datasheet).

The loop filter is located in series with the PFD and an analog switch (ADG419 of Analog Devices) controlled by the μC enables or disables the FAST loop. Downstream, an elliptic filter (LTC1562-2 of Linear Technology) can be used to reduce the laser's PZT resonance (around $161kHz$) and finally a summing stage can add an offset voltage between $0V$ and $4.5V$ to the correction signal. This offset is generated by a dual 16-bit DAC (AD5663 of Analog Devices), controlled by the μC. In order to implement the SLOW loop, one of the internal 10-bit ADCs of the μC is used to sample the output of the loop filter with a sampling rate of $10Hz$. This signal is used to compute a PID (Proportional–Integral–Derivative) servo loop which controls an external DAC, the same used in the FAST loop, whose output is sent to the Peltier cell of the laser; in Fig. 4.11 the evolution of the temperature of the Peltier cell is illustrated. Doing to temperature variations between night and day the SLOW loop corrects the frequency of the laser with oscillations of $750MHz$. The PID output spans between $\pm 8.3V$, therefore each bit corresponds to a change of about $800kHz$ in the laser frequency. The aim of the PID is to mantain the FAST correction signal near its central value

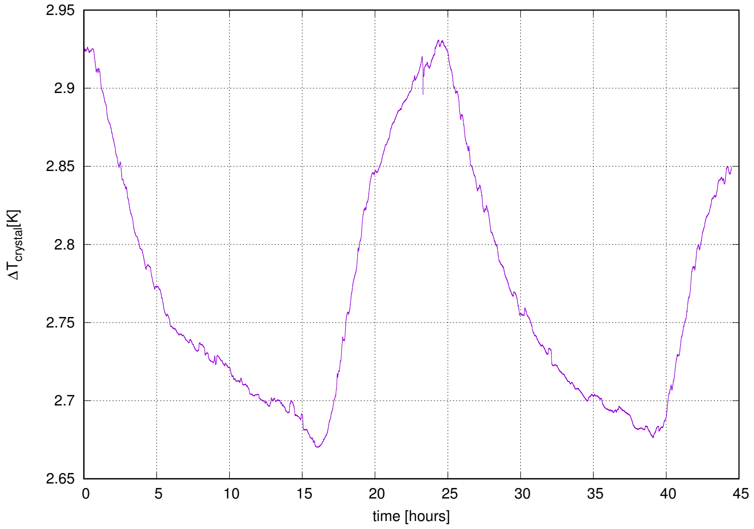

FIGURE 4.11: 2 days acquisition of the variation in the temperature of the crystal operated by the SLOW loop

($2.5V$) so that to ensure the stability of the PLL for long periods, in the order of months. An external PC is used to set the loop parameters and to monitor the state

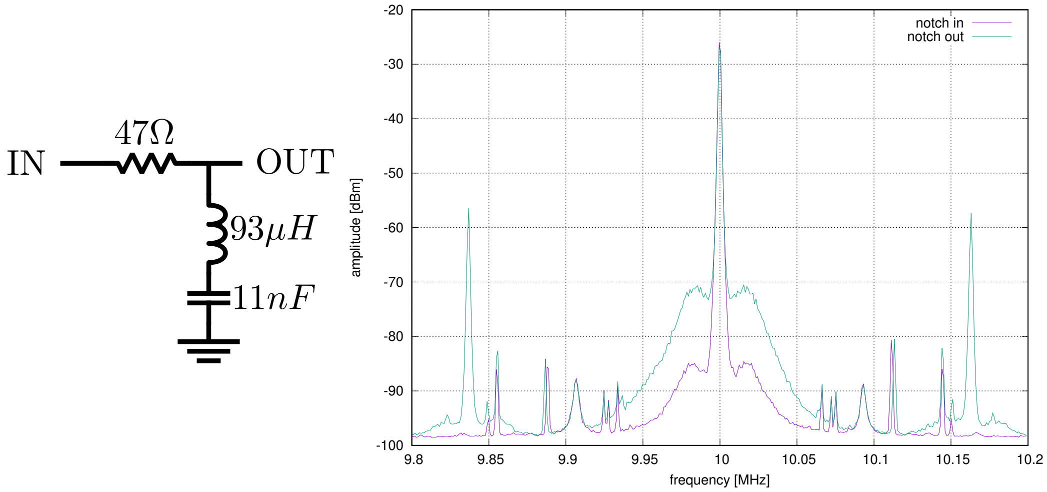

FIGURE 4.12: Notch filter circuit (left) and beat note (right) measured with a spectrum analyzer (8594E of Keysight Technologies) with span $400kHZ$, RBW $1kHz$, average over 100 measurements. The CP of the PLL was set to $I_{CP,max} \cdot 3/8$

of the μC, the communication occurs via exchange of ASCII characters using the SPI protocol. The firmware running on the μC contains a table of commands, for instance if the μC reads the string 'RE?' it returns the values stored in the latches of the PFD. A software written in Python 2.7 based on the Qt graphic libraries simplifies the serial communication between the PC and the μC.

At present, the elliptic filter is bypassed and an external RLC notch filter was designed and realized to cut the laser PZT resonance. The circuit is shown in Fig. 4.12 on the left, with the values of the components used. On the right the spectrum of the beat note is visualized with and without the filter. The peaks at $161kHz$ disappear when the notch filter is inserted between the FAST output of the PLL board and the the PZT tuning input of the laser, furthermore a reduction of the noise pedestal can be observed.

4.1.4 Phase Noise

An important parameter to be considered to evaluate the performance of a PLL in reproducing the input signal is the residual phase noise between the two lasers, $S_{\phi\phi}(\omega)$, defined [SB88] as one half of the double-sideband spectral density of phase fluctuations. Phase noise is usually expressed in dBc/Hz, where dBc are decibels relative to the carrier, because in the approximation of small phase deviations, it is equivalent to the ratio of the sideband power in a unitary bandwidth to the carrier power, see Fig. 4.13. Using the complex notation, an ideal oscillator with complex amplitude A and angular

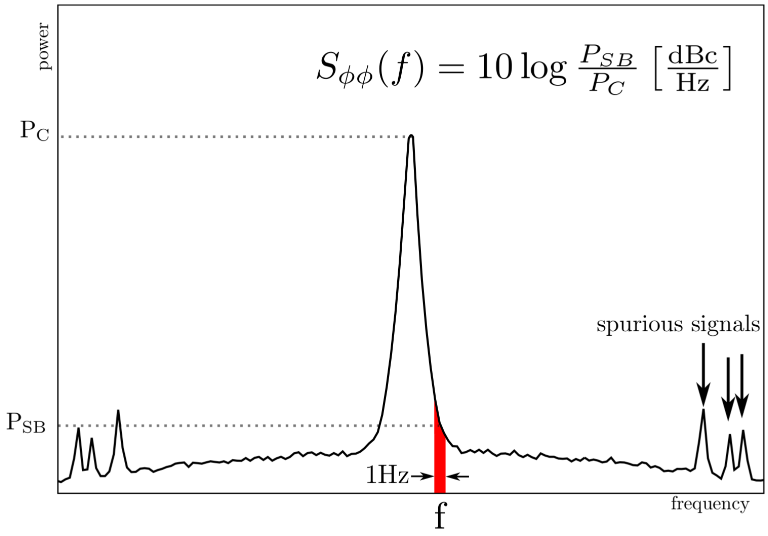

Figure 4.13: Power spectrum of a real oscillator. Discrete spourious signals are often present and they contribute to the degradation of the carrier signal

frequency ω_0 can be represented by:

$$v(t) = Ae^{i\omega_0 t}. \tag{4.11}$$

A real oscillator is affected by random phase fluctuations, $\phi_N(t)$, which are supposed to have a null mean value and a standard deviation much less than unity. Furthermore $\phi_N(t)$ is considered a weak-sense stationary process, i.e. $\langle\phi^2(t+\tau)\rangle = \langle\phi^2(t)\rangle$ for all $\tau \in \mathbb{R}$. Thus, 4.11 becomes:

$$v(t) = Ae^{i(\omega_0 t+\phi_N(t))}; \tag{4.12}$$

whose autocorrelation function is

$$\begin{aligned} R_{vv}(\tau) &\equiv \langle v(t+\tau)v^*(t)\rangle \qquad (4.13)\\ &\simeq |A|^2 e^{i\omega_0\tau}\left\langle\left(1+i\phi(t+\tau)-\frac{\phi^2(t+\tau)}{2}\right)\left(1-i\phi(t)-\frac{\phi^2(t)}{2}\right)\right\rangle \qquad (4.14)\\ &\simeq |A|^2 e^{i\omega_0\tau}(1-\sigma_\phi^2+R_{\phi\phi}(\tau)), \qquad (4.15)\end{aligned}$$

where the small angle approximation has been used. $\sigma_\phi^2 = \langle\phi^2(t)\rangle$ is the variance of phase fluctutions and $R_{\phi\phi}(\tau)$ their autocorrelation function. The power spectral density, defined as

$$S_{vv}(\omega) = \langle V(\omega)V^*(\omega)\rangle \tag{4.16}$$

where $V(\omega)$ is the Fourier transform of $v(t)$, is equal to the Fourier transform of the autocorrelation function as a result of the Wiener-Khintchine thorem [Yat14]. Thus the last expression becomes:

$$S_{vv}(\omega) = |A|^2[(1-\sigma_\phi^2)\delta(\omega-\omega_0) + S_{\phi\phi}(\omega-\omega_0)] \tag{4.17}$$

from this equation it is clear that the effect of phase fluctuations is to spread a fraction σ_ϕ^2 of the signal power to a pedestal centered on the carrier spectral line. A general theorem for stochastic process [NK03, (1.140)] shows that the area under the power spectral density curve is the mean-square error of the signal:

$$\frac{1}{2\pi}\int_{-\infty}^{\infty} S_{\phi\phi}(\omega-\omega_0)\,d\omega = \sigma_\phi^2. \tag{4.18}$$

From (4.17), $\sigma^2 \ll 1$ implies that almost all the power $|A|^2$ of the carrier is concentrated on the peak, then by definition $S_{\phi\phi}(\omega)$ is measured in dBc/Hz. On the other hand σ_ϕ^2 can be measured in $dBrad^2$ (dB relative to $1rad^2$), so by taking the integral of (4.17) over the frequencies it's easy to understand that dBc and $dBrad^2$ are equivalent units of measurement for small phase fluctuations.

The measurement of the phase noise was performed as follows: the beat note $v_{bn}(t) = A_1\sin(\omega_{bn}t+\phi_1)$ from the PD under test was demodulated with a mixer reference signal at the same frequency, $v_{ref}(t) = A_2\sin(\omega_{bn}t+\phi_2)$. The demodulated output, after low-pass filtering, was

$$v_{dem}(t) = K_{mix}v_{bn}(t)v_{ref}(t) = \frac{K_{mix}A_1A_2}{2}\cos(\phi_2-\phi_1) \tag{4.19}$$

where K_{mix} is the mixer gain. The cut-off frequency of the low pass filter was chosen to be much less than $2\omega_{bn}/(2\pi)$, but bigger than the frequency span of the measurement. The phases of input signals can be rewritten as

$$\phi_i(t) = \varphi_i + \phi_{N,i}(t), \quad i = 1,2 \tag{4.20}$$

where φ_i are the constant phase offsets and $\phi_{N,i}(t)$ are the phase fluctuations. By choosing the phase of the reference signal so that $\varphi_1 - \varphi_2 = \pi/2$ and neglecting its phase fluctuations[2], i. e. assuming $\phi_{N,2} \ll \phi_{N,1}$, 4.19 becomes

$$v_{dem}(t) = K_{dem}\phi_{N,1}(t), \tag{4.21}$$

in the approximation of small phase fluctuations, where $K_{dem} = K_{mix}A_1A_2/2$. The power spectral density of the demodulated signal, $S_{vv}(\omega)$, was measured with a FFT Network Analyzer, the SR770 of Stanford Research Systems [Sta]. Finally, the phase

---

[2] The RF generator used as reference in this work is a DDS (Direct Digital Synthesizer) AD9910 of Analog Devices. The residual phase error of the DDS is $\lesssim 19\mu rad$ RMS [Var18], much less than the residual phase error of the PLL (see Fig. 4.22)

noise was obtained using

$$S_{\phi\phi}(\omega) = \left(\frac{1}{K_{dem}}\right)^2 S_{vv}(\omega). \tag{4.22}$$

In pratcise a previous calibration is needed to convert the measured spectrum from V^2/Hz to rad^2/Hz. This is done by adding a small frequency offset $\omega_{off}/(2\pi)$ (much less than the cut-off frequency of the low-pass filter) to the frequency of the mixer reference signal. The demodulated signal thus becomes

$$v_{dem}(t) = K_{dem}\cos(\omega_{off}t + \phi_2 - \phi_1) \tag{4.23}$$

and the factor K_{dem} can be easily measured with an oscilloscope.
To develop a model of the phase noise at the output of a PLL the overall sources of noise must be considered, their effects at the output are added quadratically. There are four sources of noise which affect the PLL performance [CO99]: the phase noise of the reference input S_{REF}, the noise due to the feedback divider[3], the noise due to the charge pump S_{CP} and the noise of the VCO, i.e. of the two lasers, S_{VCO} (see Fig.4.14). The total phase noise power at the output of the loop is

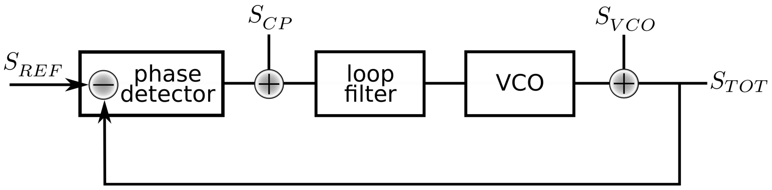

FIGURE 4.14: contributions to the total phase noise of a PLL

$$S_{TOT}^2 = X^2 + Y^2 + Z^2 \tag{4.24}$$

where to compute the various contributions the transfer function of the PLL (4.10) is used as follows:

$$\begin{cases} X^2(s) = H^2(s)S_{REF}^2(s) \\ Y^2(s) = \left(\frac{1}{K_{pd}}\right)^2 H^2(s)S_{CP}^2(s) \\ Z^2(s) = \left(\frac{s}{K_{VCO}K_{pd}F(s)}\right)^2 H^2(s)S_{VCO}^2(s) \end{cases} \tag{4.25}$$

The contributions of S_{REF} and S_{CP} are low-pass filtered, in fact inside the loop bandwidth $|H(s)| \simeq 1$ while at high frequencies $|H(s)| \to 0$ (see Fig. 4.9). Vice versa S_{VCO} is high-pass filtered by its transfer function. The effect is that the noise of the VCO dominates at high frequencies, while the other two contributions are higher at low frequencies. The effects of the three contributions superimposed to a measure of the

---

[3] in this experiment the reference divider was not used, so this contribution will be neglected

phase noise are shown in Fig. 4.15, the input phase noises are referred to the datasheet of the devices used: the REF was the AD9910 of Analog Devices, the VCO was the Mephisto of Coherent and the CP was the charg pump of ADF4002 of Analog Devices.

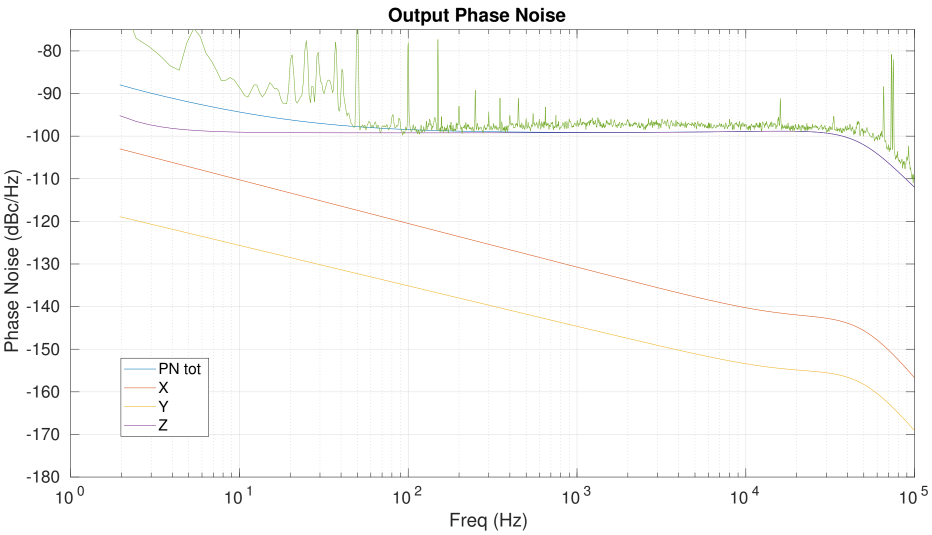

FIGURE 4.15: Predicted and measured phase noise of the PLL @10MHz

4.2 Optical Bench

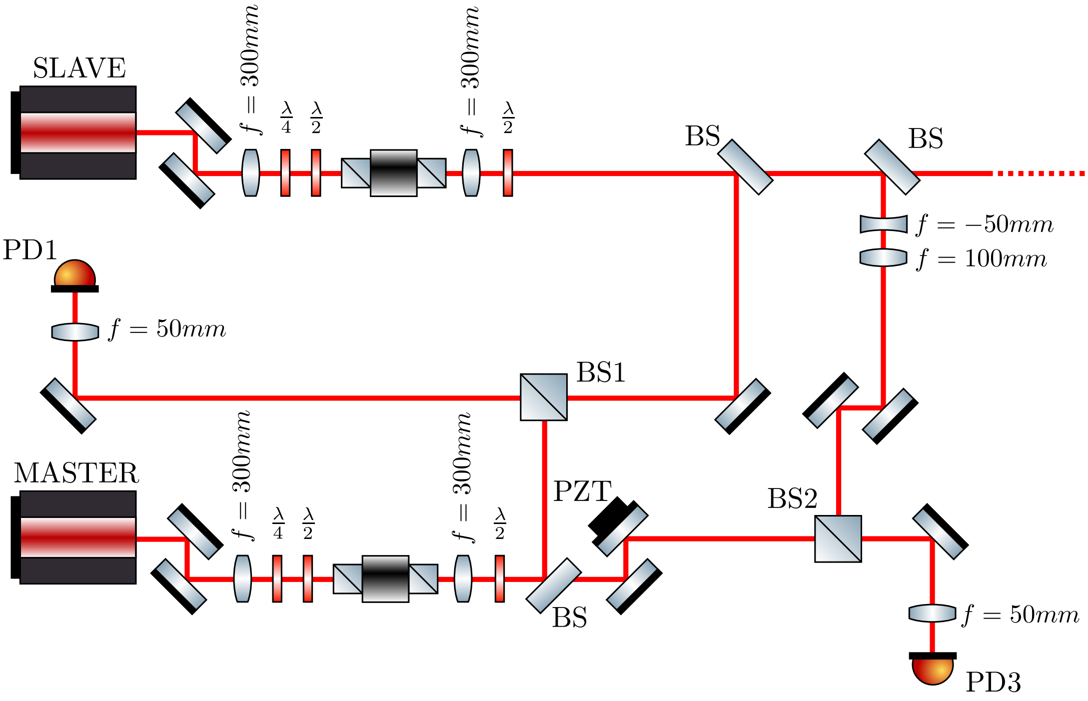

FIGURE 4.16: Schematic of the Optical bench

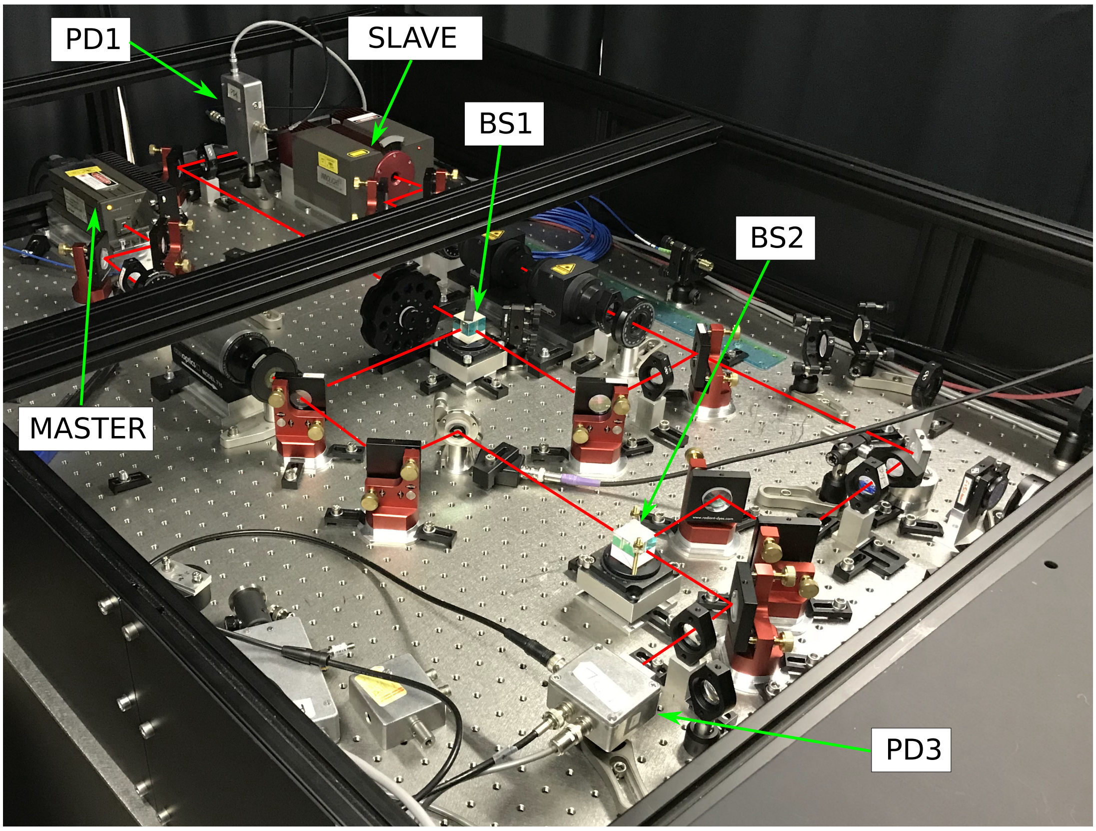

FIGURE 4.17: Picture of the bench realized at LNL, the principal components are highlighted

Fig. 4.16 shows how the optical setup to test the stability of the control system was realized. The two laser beams are superposed using a BS in two different points of the optical path: the beat note from their interference in BS1 was used to close the OPLL (see §4.1), whereas the beat note from BS2 is sensitive to the additional phase noise caused by the beam propagation after the locking on PD1 and was demodulated to obtain the error signal for the second loop. PD1 and PD3 were used to detect these signals respectively. The lasers used in the experiment were a $50mW$ Lightwave as master and a Mephisto of Coherent as slave. The following table summarizes the Mephisto main properties:

Wavelength	$1064nm$
Power	$0.5W$
Crystal	monolithic Nd:YAG
Thermal Tuning Coefficient	$-3GHz/K$
Thermal Tuning Range	$30GHz$
Thermal Response Bandwidth	$\sim 1Hz$
Temperature Laser Crystal	$1K/V$
PZT Tuning Coefficient	$\sim 2MHz/V$
PZT Tuning Range	$\pm 65MHz$
PZT Response Bandwith	$100kHz$

To add an arbitrary phase noise between the two beams a piezo-mounted mirror was placed on the path of the master laser so that the optical path could be modulated at different frequencies, in order to measure the bandwidth at which the feedback network is able to correct the noise. A picture of the optical bench realized in the clean room of LNL shows the principal components, see Fig. 4.17, the bench is surrounded by protective screens realized in anodized aluminium and can be covered to reduce enviromental noises.

4.2.1 Characterization of the Piezoelectric Actuator

A characterization of the PZT on which the mirror is mounted is important to properly design the control system; particularly, its dilation coefficient K_{PZT} (in units of nm/V) and its frequency response have to be measured.

The mount for the mirror is a commercial model which hosts an adapter for the PZT, a P-016.00H of PI [Phy], with tabulated dilation coefficient $K_{PZT} = 5nm/V$ and resonant frequency $144kHz$. The mirror is directly glued onto the PZT using Stycast 2850 FT (see. Fig4.18). The measurement of the dilation coefficient was done as follows. First, the slave laser was locked to the master with an OPLL at $10MHz$, then a triangular function at frequency $\hat{f} = 100Hz$ and amplitude $\hat{V}_{pp} = 4.85V$ was applied to the PZT after being amplified by factor ×100. The signal from PD3, demodulated at $10MHz$, was proportional to the sine of the phase difference between the laser beams, i.e. to $\sin[\frac{2\pi}{\lambda}\sqrt{2}K_{PZT}\alpha t]$, where $\lambda = 1064nm$ was the wavelength of the lasers and $\alpha = 2\hat{f} \cdot 100\hat{V}_{pp}$ was the slope of the rising ramp of the triangular signal. The factor $\sqrt{2}$ comes out from the geometry of the system, see Fig. 4.19. Both the triangular function and the demodulated signal were observed through an oscilloscope (LeCroy LT342, see Fig. 4.20). The response of a PZT ring actuator is not linear, therefore we have characterized it in the region in which it is supposed linear (small input voltage). Thus the window of measurement was reduced to the central part of the rising ramp

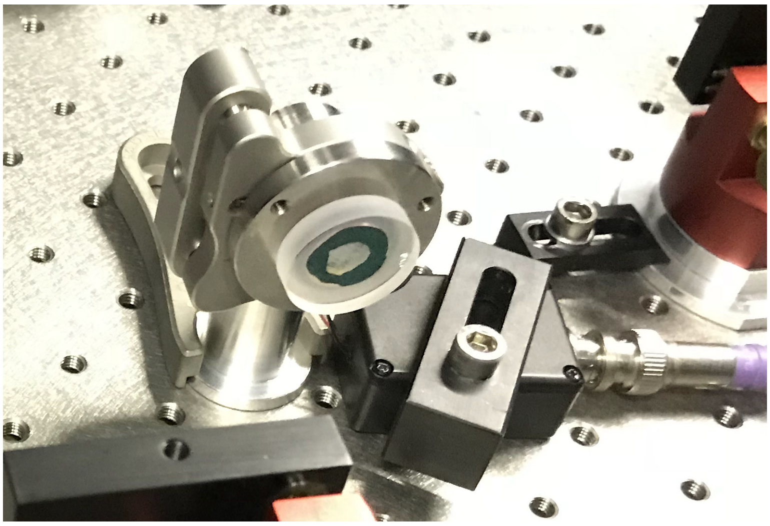

FIGURE 4.18: Picture of the mount of the mirror piloted with the PZT ring actuator. The black box on the right hosts the SHV connector for the HV cable

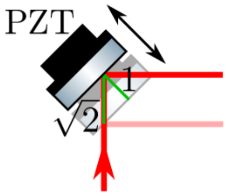

FIGURE 4.19: Geometry of the optical path of the laser beam when it is reflected by the moving mirror

of the triangular signal. Finally, the period T of the sine was computed averaging 1000 measurements and it is equal to $T = (1.580 \pm 0.005) ms$. Thus from the relationship $\frac{2\pi}{\lambda}\sqrt{2}K_{PZT}\alpha T = 2\pi$ one obtains

$$K_{PZT} = \frac{\lambda}{\sqrt{2}\alpha T} = (4.91 \pm 0.02)\frac{nm}{V}. \tag{4.26}$$

The measurement of the transfer function of the PZT was performed with a network analyzer (SR770 of Stanford Research Systems): this instrument includes a DDS source which can generate a chirp composed by 400 discrete sine waves of equal amplitudes and with equally spaced frequencies in order to cover the entire selected span of the spectrum. The source is synchronized with the input of the instrument so that the SR770 can measure amplitude and phase transfer curves for a device under test, after a preliminary calibration of the chirp phases and amplitudes. The autocalibration is necessary beacause the SR770 has only one input channel. The network under test consists in the chain: HV amplifier ×100 - PZT - PD3 - mixer (Minicircuit ZP-10514+) - low-pass filter with cut-off frequency $210kHz$. A series of 9 measurements was performed in order to have roughly the same number of points per decade of frequency, choosing every time a span which was half the value of the last one, from

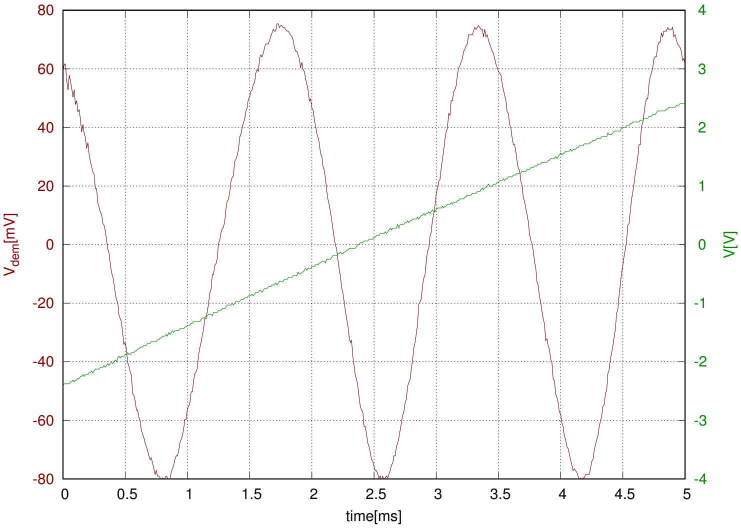

Figure 4.20: Response of the PZT to a triangular input. In green the triangular function before amplification, in red the demodulated signal

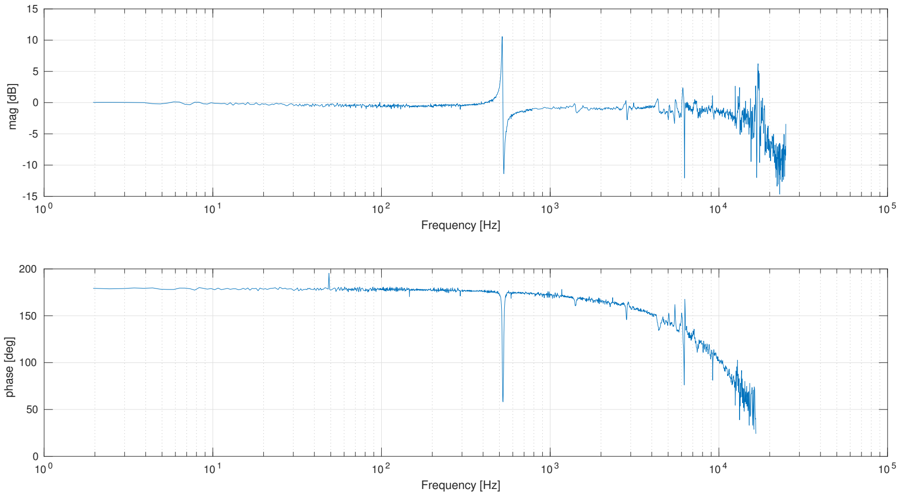

Figure 4.21: Bode plot of the PZT transfer function. In order to know the exact value of the optical path change, the magnitude must be multiplied for $\frac{2\pi}{\lambda}\sqrt{2}K_{PZT}V_{app}(f)$, where $V_{app}(f)$ is the voltage applied at frequency f

$100kHz$ to $390Hz$; the final Bode plot was obtained by superimposing the various sets of data, as shown in Fig. 4.21. The transfer function is almost flat up to $\simeq 10kHz$, beyond that value the response begin to fall beacause of the RC low-pass filter composed by the output impedence of the piezo driver and the PZT capacitance. A resonance is present at $519Hz$, but its origin is presently unknown. Probably it is a mechanic resonance.

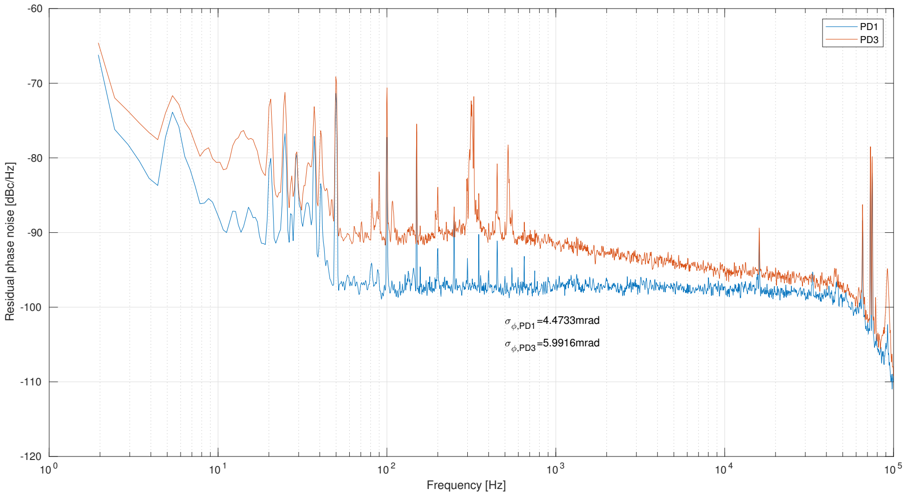

Figure 4.22: PLL phase noise measured in two different points of the bench (PD1 and PD3, see Fig. 4.16). The $2Hz$ to $100kHz$ values of RMS σ_ϕ are also shown. The PLL was locked at $10MHz$

4.3 Phase Control Loop

A measure of the phase noise (see Fig. 4.22) was performed by taking the signal of the beat note with two PDs placed at different distances from the lasers, the OPLL being locked with the signal from PD1. From the values of the integrals below the curves, i.e. rms value of the phase fluctuations (computed between 2 Hz and 100 kHz), it is clear that near the point of locking the fluctuations are smaller than those at long distance, due to enviromental noises which affect the phase at low frequencies. The goal of this thesis is to reduce these fluctuations at low frequencies in order to obtain a stabilization of the phase difference between the two laser beams at a point far away from the sources. The conceptual model of the phase control loop is shown in Fig. 4.23, the names of the BSs and of the PDs are the same of Fig. 4.16. The OPLL ensures the two laser beams to have the same phase in the point where PD1 is placed, but when they are overlapped in PD3 a certain amount of phase difference has been accumulated due to the different optical paths (static contribution) and to mechanical and acoustic noise (dynamical contribution). This difference is indicated as ϕ_N in the figure and can be measured by demodulating the signal from PD3 at the offset frequency of the OPLL, in the same way we obtained (4.21). Note that in the optical bench realized for this thesis ϕ_N can be piloted with a signal applied to the PZT-mounted mirror placed in the path of the master laser beam[4]. The control loop can be closed by acting on the phase of the OPLL reference signal in order to compensate the disturbance ϕ_N.

---

[4] actually, ϕ_N should be the sum of the noise introduced with the PZT and of the enviromental noise, but if the signal applied to the PZT is strong enough the last term can be neglected

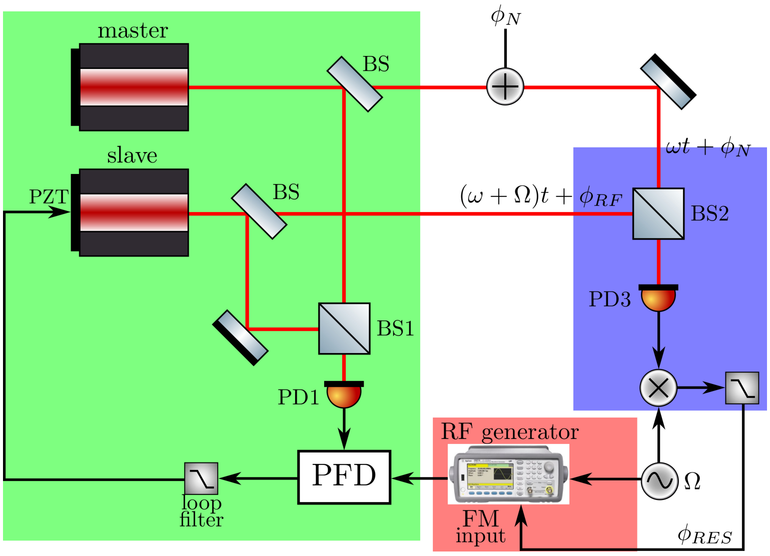

FIGURE 4.23: Sketch of the control loop. The green square includes the components of the OPLL, the blue square includes the demodulation components employed to read the phase difference between the two laser beams and the red square include the stadium for the FM

The demodulated signal from PD3 is used to actuate on the phase/frequency of a radio frequency (RF) generator (33521A of Keysight Technologies[Key]) by means of its modulation input. This RF generator is phase locked on the DDS generator system used both as PLL reference and for the error signal demodulation. The RF generator output can be modulate either in phase (PM) or in frequency (FM). The modulation in frequency was chosen for two reasons:

- the maximum phase deviation for the PM is 2π radians, while the FM has no limitations for the phase deviation of the output signal;
- the correction signal with PM has a white spectrum, while with FM it is stronger at low frequencies. In fact, the angular frequency deviation is the time derivative of the instant phase deviation $\Delta\omega(t) = \frac{d\Delta\phi(t)}{dt}$ and passing to the frequency domain one obtains $\Delta\phi(s) = \frac{\Delta\omega(s)}{s}$. This is a desired behaviour because the seismic noise, which is the dominant contribution to the residual phase noise between the ITF laser and the QCF in Virgo, dominates at very low frequencies: the power linear density of the micro-seismic noise is proportional to f^{-2} [Mag07, 9.4.4].

The error transfer function $ERR(s) = \phi_{RES}/\phi_N$ is now studied, where ϕ_{RES} is the residual phase difference between the two fields at PD3 when the control loop is active. The goal of the control system is to keep ϕ_{RES} as low as possible. The block diagram of the loop is shown in Fig. 4.24, for each block the transfer function in the frequency domain is shown. The colours of the blocks are refferred to those employed in Fig. 4.23. $G(s)$ represents the demodulation of the beat note from PD3, i.e. it is the combination

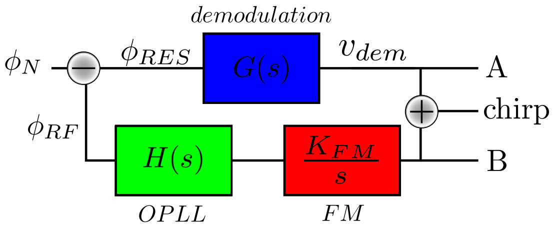

FIGURE 4.24: block diagram of the phase control loop, the disturbance rejection is the ratio between ϕ_{RES} and ϕ_N. In the picture is present the summing point used for the measure of the OLTF, in the operating configuration of the loop this element was removed

of the mixer response ($ZP-10514+$ of Minicircuit) and of the filter, which is a passive first order low-pass filter with cut-off frequency of $210kHz$[5]. Thus:

$$G(s) = \frac{K_{dem}}{1 + \frac{s}{2\pi 210kHz}} \tag{4.27}$$

where K_{dem} is the conversion factor of the demodulation (cf. (4.21)). K_{FM}/s is the transfer function of the FM, where K_{FM} is the frequency deviation per volt applied to the modulation input of the RF generator, for the measurements presented in this work an optimal value of $k_{FM} = 20kHz/V$ was chosen. $H(s)$ is the CLTF of the OPLL, as described in §4.1.2.

The OLTF was measured to characterize the system, the spectrum analyzer SR770 of Stanford Research System was used. The chirp function (described at the end of the previous section) was employed as follows: the signal produced by the SR770 was injected in the summing point depicted in Fig. 4.24 and the transfer curves were measured at points A and B. To obtain the magnitude of the OLTF the magnitude curve measured in A was divided by the magnitude curve measured in B, while the phase of the OLTF was found by subtracting the phase curve measured in B from the phase curve measured in A. The resulting curves are shown in Fig. 4.25 (blue lines). The phase is affected by a rotation which is not predicted by the model, but is compatible with a time delay of $18\mu s$ in the loop line. Since the loop is composed by analog elements with the exeption of the RF generator, the research of the delay was focused on this element. In order to study the response velocity of the RF generator to a change in the applied modulating voltage, a square-wave signal at $100Hz$ was directly applied to the modulation input. The maximum value of the square wave was set to $2V$ (corresponding to a frequency variation of $40kHz$) and its minimum value was set to $0V$ (no frequency modulation). The output signal of the RF generator, operating at a carrier frequency of $10MHz$, was then demodulated at $10MHz$ and low-pass filtered with a cut-off frequency of $210kHz$, in order to keep only the frequency variations

---

[5] The contribution of PD3 to the frequency response can be neglected in the frequency region of interest, being the measured banwidth of the PD (FCI-InGaAs-500 of OSI Optoelectronics) and its circuit of about $45MHz$

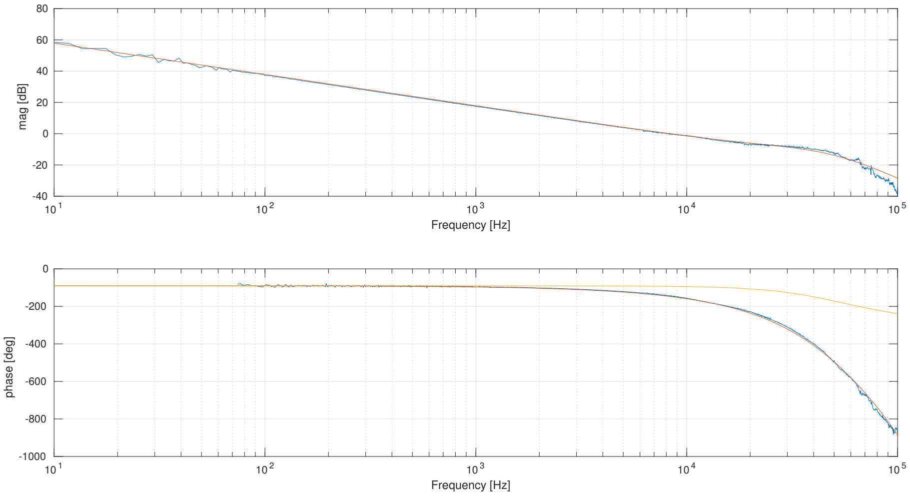

FIGURE 4.25: Bode plots of the measured OLTF (blue lines). The yellow line represents the predicted phase of the transfer function, the red lines represent the model with the delay element

induced by the FM. The square wave and the demodulated signal were observed at the oscilloscope (LeCroy LT342) and by zooming around the rising edge of the square wave the time delay of the step response was measured, see Fig. 4.26. The measured delay is $(16 \pm 1)\mu s$, compatible with the predicted value. The complete OLTF is than

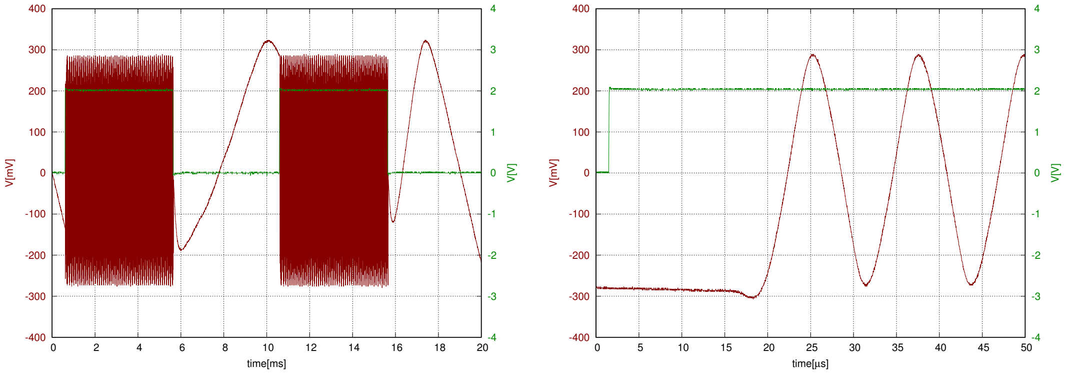

FIGURE 4.26: Left: square wave (green line) used as modulation signal to study the delay of the frequency modulation (red line). Right: zoom ×400 of the time axis to visualize the step response

$$T_{OL}(s) = \frac{K_{FM}}{s} e^{-s\tau} H(s)G(s) \tag{4.28}$$

where τ is the delay due to the digital FM. In figure 4.25 the curves with and without the delay element are superimposed to the experimental data. It is worth noting that the amplitude of the OLTF is not affected by the delay, while the closed loop is strongly influenced by the phase rotation. The unity gain bandwidth is $8.3kHz$ and the phase margin is 33°. From T_{OL} the error transfer function can be calculated by using

$$ERR(s) = \frac{1}{1 + T_{OL}(s)}, \tag{4.29}$$

whose amplitude is shown in Fig. 4.27; the (unwanted) peak at $11.8 kHz$ is a consequence of the delay element in the loop. The model provides a noise rejection at frequencies lower than $6.1 kHz$, with a slope of $20 dB/dec$, as expected from the DC pole:

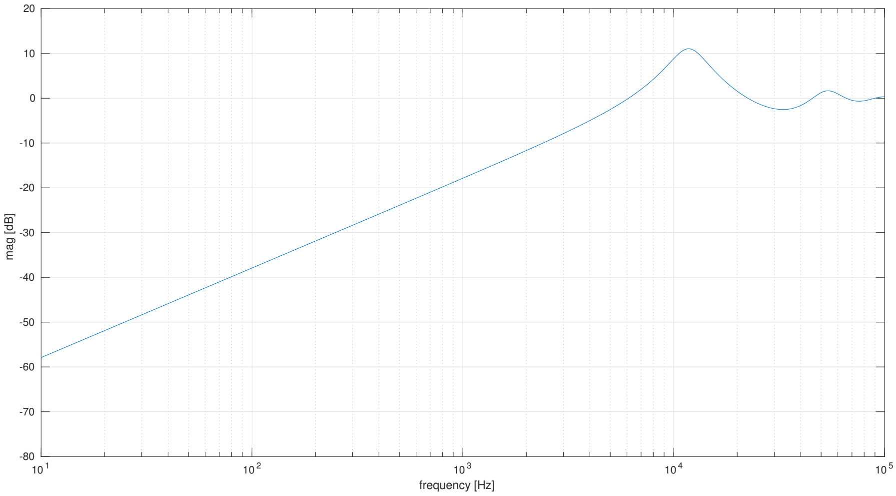

FIGURE 4.27: amplitude plot of the error transfer function

$$T_{OL}(s) \xrightarrow{s \to 0} \frac{1}{s} \qquad \Rightarrow \qquad ERR(s) \xrightarrow{s \to 0} s. \tag{4.30}$$

Given the residual phase noise $S_{\phi_N \phi_N}(s)$ entering the loop in the propagation of the two laser beams, the phase noise at PD3 when the control loop is active is given by

$$S_{\phi_{RES} \phi_{RES}}(s) = |ERR(s)|^2 S_{\phi_N \phi_N}(s). \tag{4.31}$$

This relation was tested by injecting white noise in the PZT on which the mirror is mounted, and than measuring the attenuated phase noise at PD3 with the control loop turned off, obtaining $S_{\phi_N \phi_N}(s)$, and with the control loop turned on, obtaining $S_{\phi_{RES} \phi_{RES}}(s)$ (see Fig. 4.28). The white noise, produced by a function generator (DS345 of Stanford Research System) in a bandwidth of $10 MHz$ and with $V_{RMS} = 1V$, was amplified ×100 before being fed to the PZT. The low-pass response of the combination piezo driver + PZT (see §4.2.1) cut the noise frequencies above $\sim 10 kHz$. Below $\sim 100 Hz$ the reduced noise increases, this is due to the presence of other noise sources in the loop, expecially electrical noises, which are not suppressed and adds their contriutions to the final noise, covering the expected noise rejection. The injected white noise had a level of $1V$ distributed over a $10 MHz$ band. In order to study the efficiency

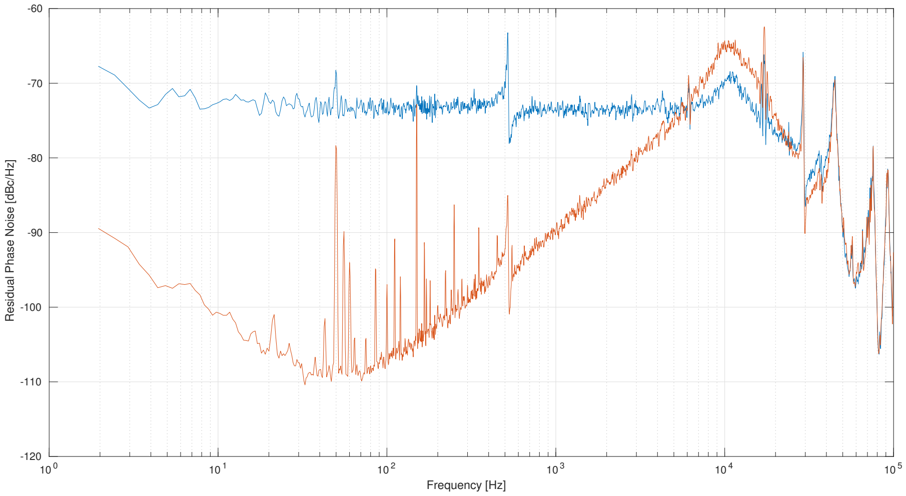

Figure 4.28: Phase noise measurement of the injected white noise (blue line) and of the reduced noise (red line)

of the filtering system at low frequency it is necessary to increase the amplitude of the displacement injected by the PZT. Unfortunately, however, this can not be achieved by simply increasing the white noise level of the function generator because the RMS value injected in such a way is higher than the level accepted by the HV piezo driver. The white noise used, however, is distributed over a band which is excessive if one wants to study the low frequency behavior. The white noise was than low-pass filtered, thus reducing the RMS voltage. This ensured that under these conditions the total RMS value injected into the piezo driver was considerably lower and therefore the absolute value could be increased without exceeding the HV range. In particular, using a cut-

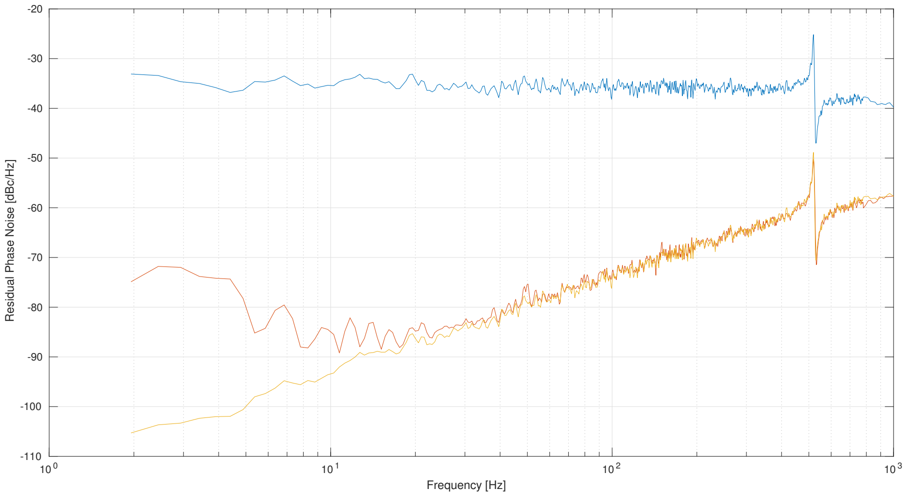

Figure 4.29: Phase noise measurement of the injected white noise (blue line) and of the reduced noise (red line). The yellow line represents the predicted noise rejection and was obtained by using (4.31)

off frequency of $1kHz$, the injection value could be amplified by a factor ×40. The injected noise curve and the reduced noise curve are shown in Fig. 4.29. Again, a consistent difference between the measured and the predicted reduced noise is present, at frequencies below $20Hz$, to explore lower frequencies a higher excitation is required. In the region between $20Hz$ and $1kHz$ the measured curve is well superposed to the expected results, confirming that the model developed in this section is consistent. Note that the injected noise curve $S_{\phi_N \phi_N}$ was derived by measuring the power spectral density of the injected white noise and by multiplied it by the tranfer function of the PZT: $S_{\phi_N \phi_N}$ is not simply the phase noise measured in PD3 when the loop is turned off because the amplitude of the fluctuations induced by the vibrating mirror are too large to consider the linear approximation $sin(\phi_N) = \phi_N$, in fact the RMS phase fluctuation injected by the mirror was $580mrad$.

Chapter 5

Conclusions

In this work a first prototype for the squeezing ellipse angle control has been designed and realized. In a real interferometer this type of control loop is required to lock the phase of the squeezed light to that of the ITF carrier. In this regard, the main sources of disturbance acting on the system are the following (see Fig. 5.1):

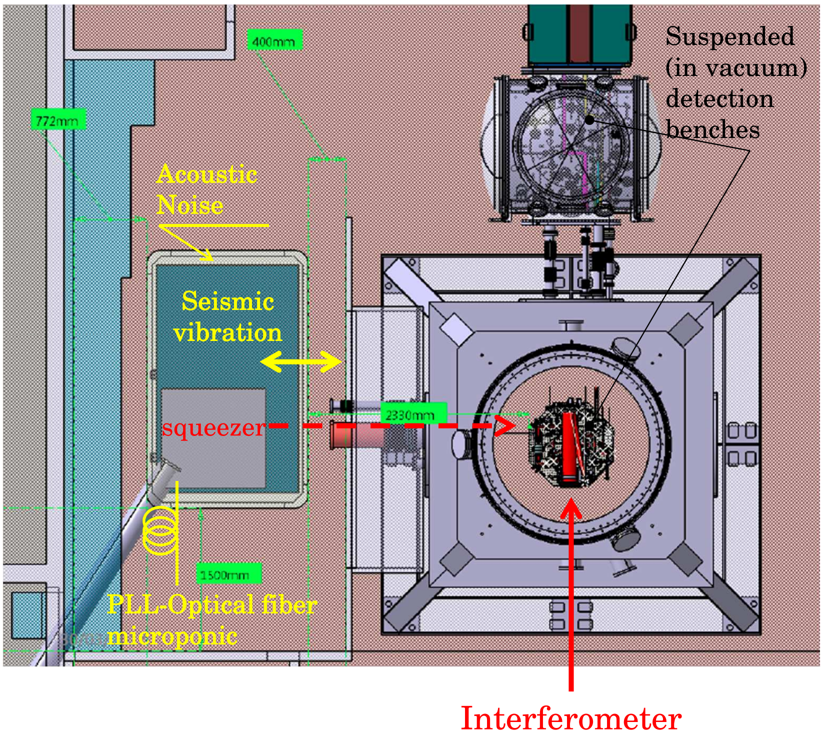

FIGURE 5.1: Principal phase noise sources between the squeezed light and the ITF light

- the squeezing bench is anchored to the ground and than vibrates with an amplitude Δx_{seism} equal to the displacement caused by the seismic noise. This induces a phase noise between the squeezed light and the carrier equal to $\Delta\phi_{seism} = \frac{2\pi}{\lambda}\Delta x_{seism}$, where $\lambda = 1064nm$ is the wavelength of the laser;

- To close the OPLL between the Virgo laser and the main laser of the squeezer bench, an optical fiber is used in which a pick-off of the virgo main laser is injected. The fiber ($50m$ long) is located in the central building between the injection Lab and the detection Lab, where can pick-up ambiental thermo and acoustical noise which is transferred to the main laser of the squeezer bench;
- Although the squeezer is installed in an acoustic enclosure that absorbs frequencies up to few hundreds Hz, it is still subject to environmental noise.

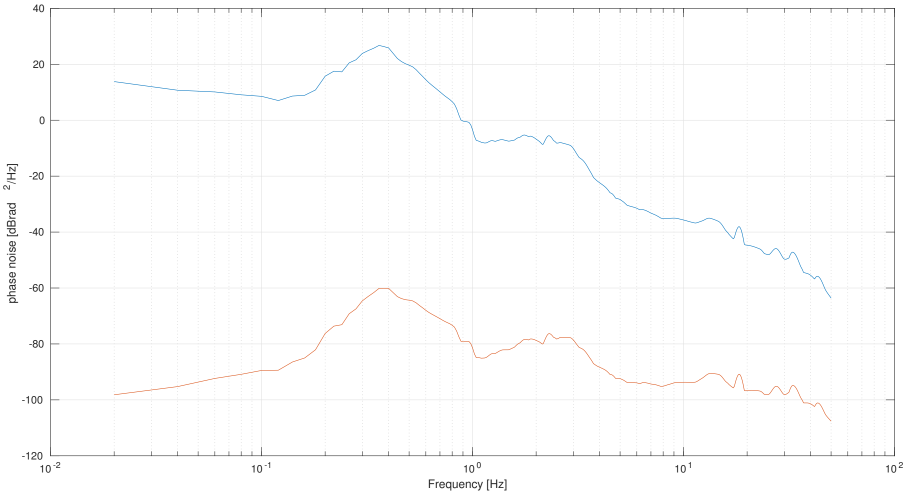

Figure 5.2: Phase noise $S_{\phi_{seism}\phi_{seism}}$ obtained from the PSD of the seismic displacement $S_{\Delta x_{seism}\Delta x_{seism}}$ measured in the proximity of the Virgo interferometer (blue line) and the expected reduction operated by the phase control loop (red line). The blue plot was derived by means of $S_{\phi_{seism}\phi_{seism}} = (2\pi/\lambda)^2 S_{\Delta x_{seism}\Delta x_{seism}}$. The parameters set in order to simulate the phase control loop are the same used in §4.3

As an example let consider the seismic noise measured where the Virgo ITF is placed (see Fig.5.2), the micro-seismic peak [Bat13] can be seen in the plot at $360mHz$. The RMS phase fluctuation is $8.76rad$ between $20mHz$ and $50Hz$; With the loop developed in this thesis, this value can (in principle) be reduced to $0.5mrad$ in the same band of frequencies. Thus the phase control loop is able to reduce this contribution below our requirement ($20mrad$ RMS, see 3.2.1). However this is only a lower limit, because the other contributions (thermo and acoustic noise from the optical fiber and enviromental noise on the squeezing bench from the non perfect acoustic enclosure), as well as the sensing noise, has not been included in this calculation, thus an higher residual phase noise is expected. The actual phase noise will be estimated when the squeezer will be installed in the Virgo detector. In this case it would be required to adapt the loop transfer function to the real noise.

Finally the delay time must be minimized, if a larger bandwidth is required for the loop. In fact the delay is responsible for the increased noise at frequencies above $6kHz$, as shown in Fig. 5.3, so residual acoustic noise could be amplified affected the stability of the loop.

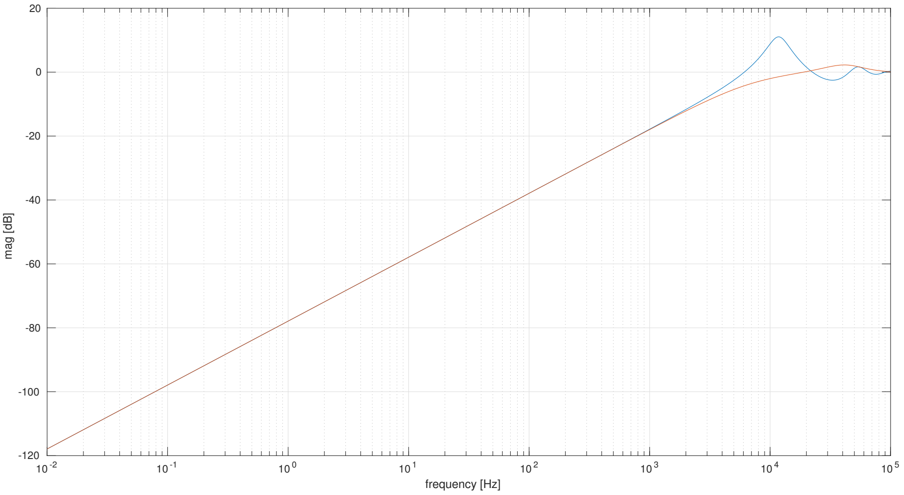

FIGURE 5.3: rejection ratio of the noise with the delay element (blue line) and without delay (brown line)

Appendix A

Appendix: OPLL board

The circuit diagram of the OPLL board is displayed in Fig. A.1, Fig. A.2, Fig. A.3 and Fig. A.4. In particular Fig. A.1 shows the beat note and the local oscillator input stages and the phase frequency detector. The components C1, C10 and R6 are the loop filter components and have to be adapted to each OPLL control loop. Fig. A.2 shows the fifth order Bessel filter that attenuates $20dB$ in the bandwidth between 100 and $200kHz$ with the aim to suppress the laser's piezoelectric mechanical resonance. Moreover in this second sheet is placed the digital switch that allows to turn on/off the FAST loop. The third sheet in Fig. A.3 shows the ADC, the DAC and the operational amplifiers that prepare the FAST and the SLOW output signals. Finally the fourth sheet in Fig. A.4 contains all the voltage regulators and the microcontroller unit. This board was designed by Marco Prevedelli.

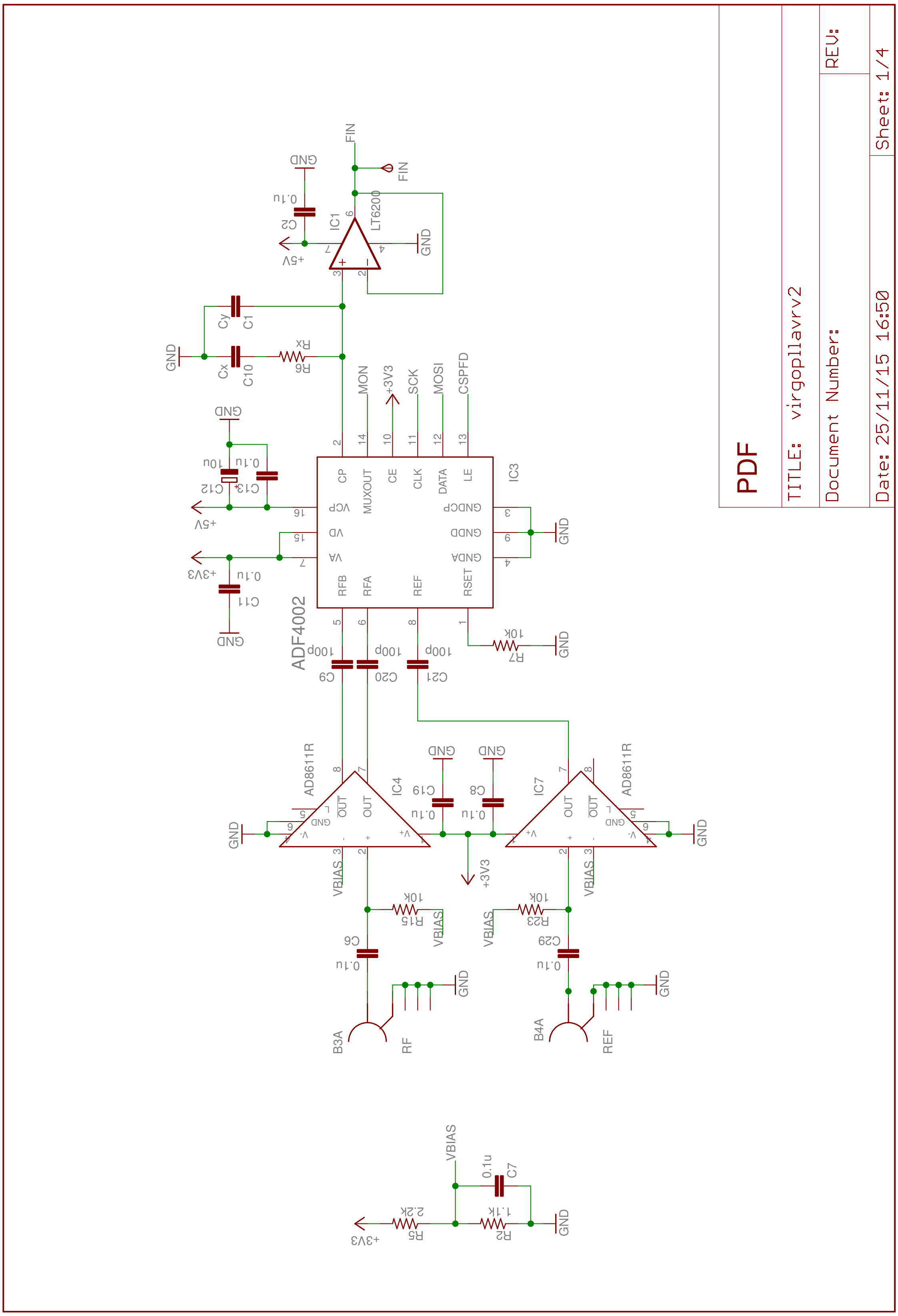

Figure A.1: OPLL circuit diagram sheet 1/4

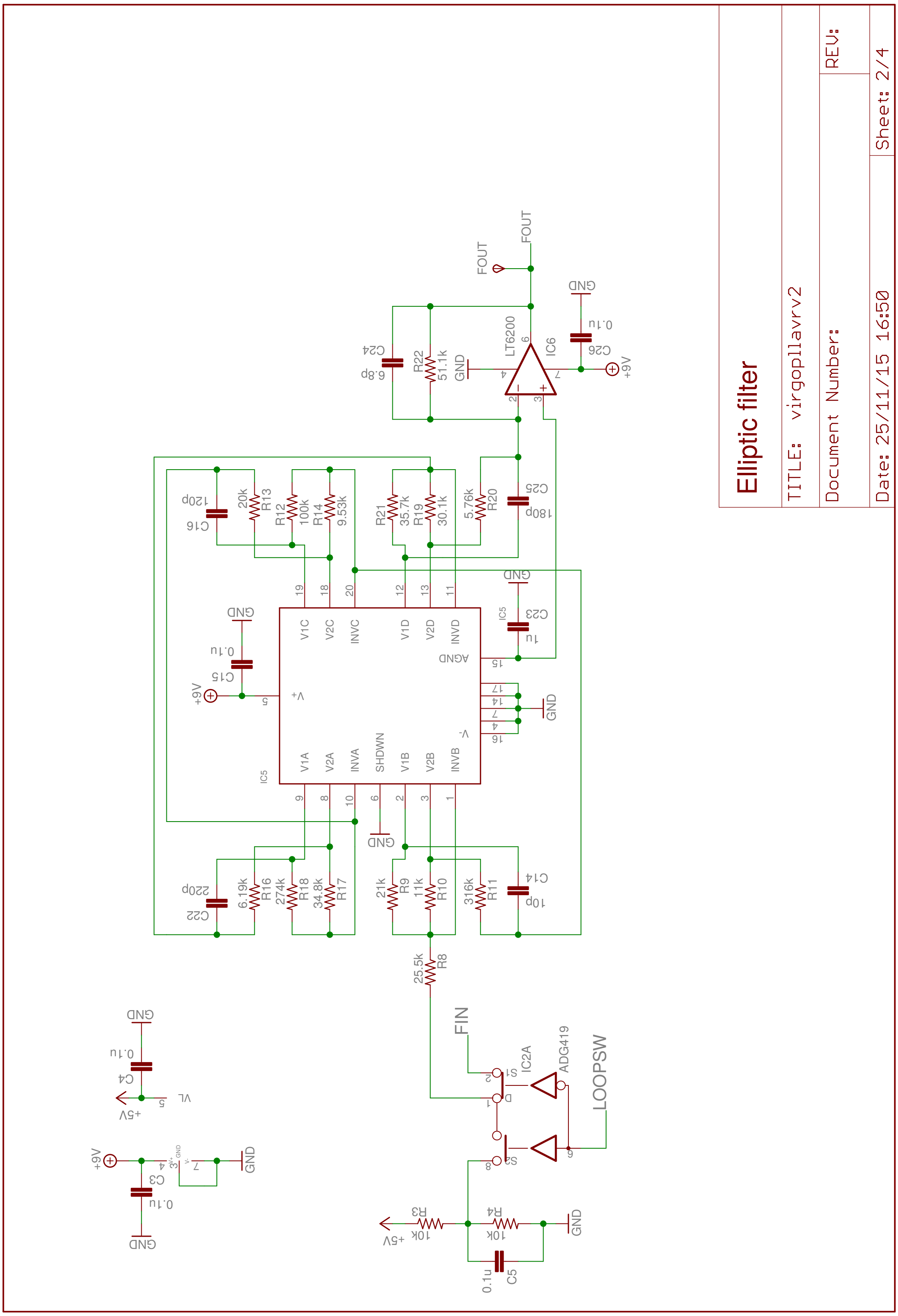

Figure A.2: OPLL circuit diagram sheet 2/4

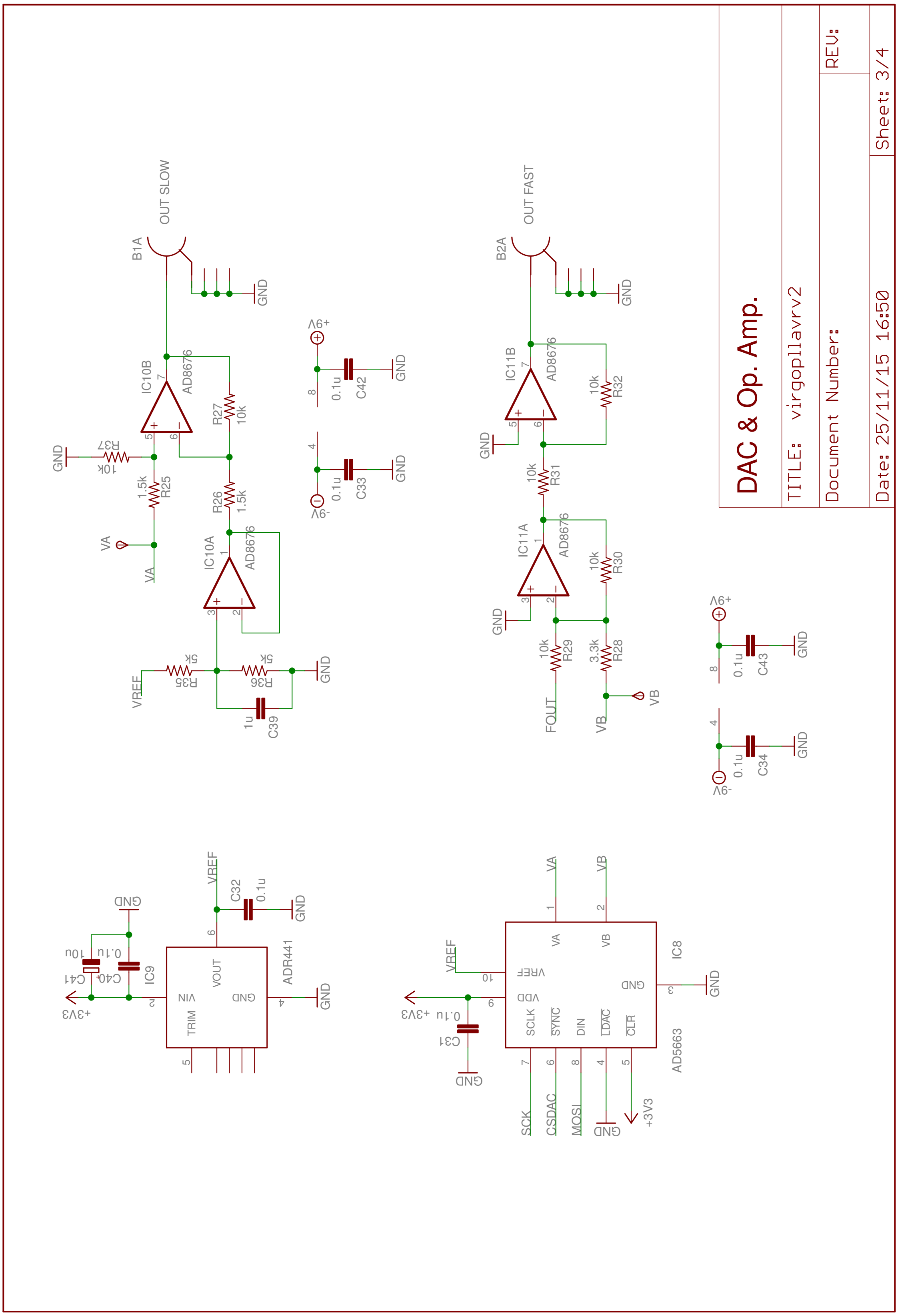

Figure A.3: OPLL circuit diagram sheet 3/4

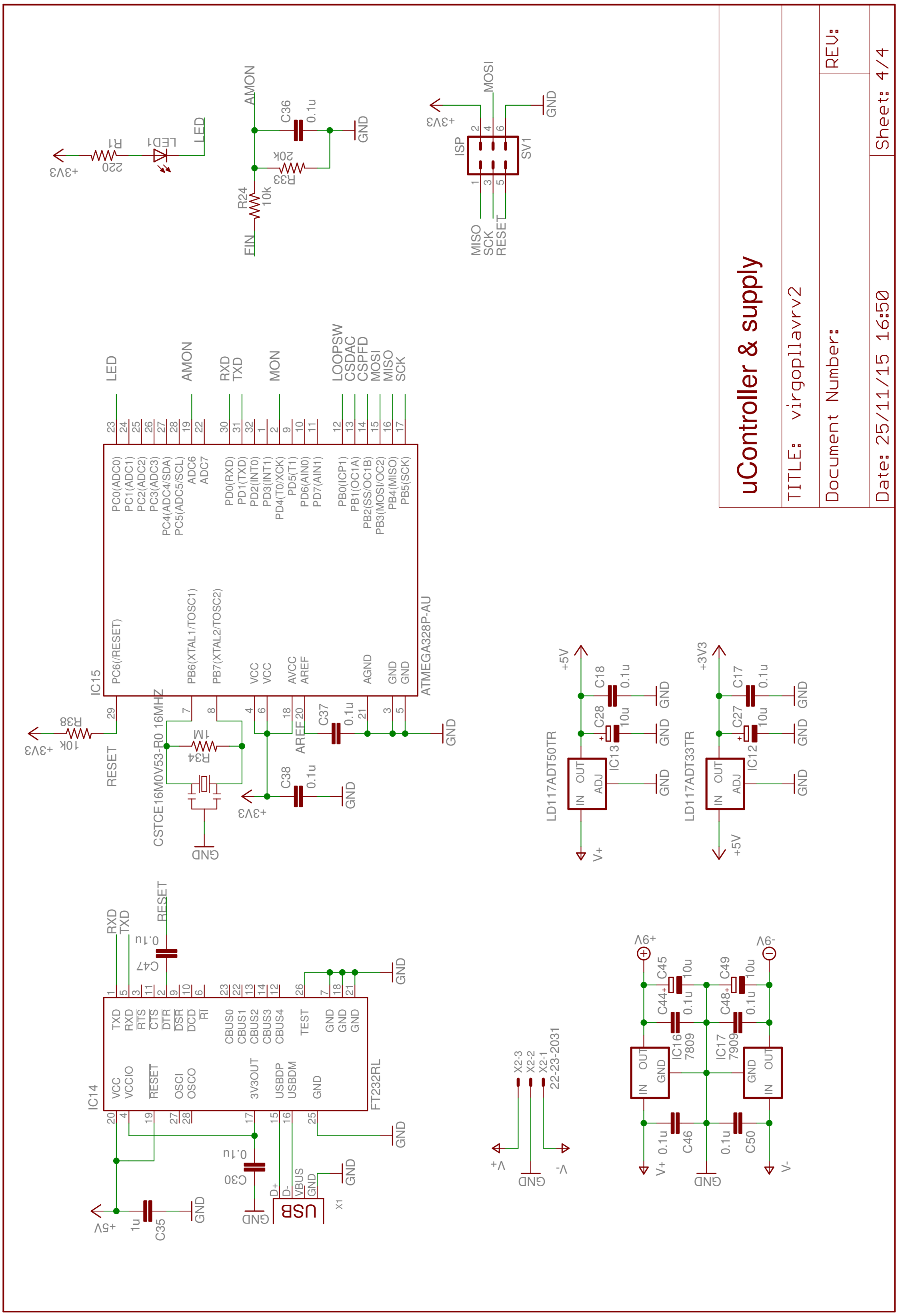

FIGURE A.4: OPLL circuit diagram sheet 4/4

Bibliography

[AD05] Peter Aufmuth and Karsten Danzmann. Gravitational wave detectors. *New Journal of Physics*, 7(1):202, 2005.

[Ana] Analog Devices. *ADIsimPLL*. https://form.analog.com/form_pages/rfcomms/adisimpll.aspx.

[Ana15] Analog Devices. *ADF4002 - Phase Detector/Frequency Synthesizer*, 2006-2015. D06052-0-9/15. http://www.analog.com/media/en/technical-documentation/data-sheets/ADF4002.pdf.

[Bat13] M. Bath. *Introduction to Seismology*. Wissenschaft und Kultur. Birkhäuser Basel, 2013.

[Boy03] R.W. Boyd. *Nonlinear Optics*. Elsevier Science, 2003.

[BR04] H.A. Bachor and T.C. Ralph. *A Guide to Experiments in Quantum Optics*. Wiley, 2004.

[Cav81] Carlton M. Caves. Quantum-mechanical noise in an interferometer. *Phys. Rev. D*, 23:1693–1708, Apr 1981.

[Che07] Simon Chelkowski. *Squeezed light and laser interferometric gravitational wave detectors*. PhD thesis, Gottfried Wilhelm Leibniz Universität Hannover, 2007.

[CO99] Mike Curtin and Paul O'brien. Phase-locked loops for high-frequency receivers and transmitters—part 2. *Analog Dialogue*, 33(5):1–4, 1999.

[Coh] Coherent Lasers. *Mephisto/Mephisto S*. https://edge.coherent.com/as1sets/pdf/COHR_Mephisto_DS_0417_2.pdf.

[CS85] Carlton M. Caves and Bonny L. Schumaker. New formalism for two-photon quantum optics. i. quadrature phases and squeezed states. *Phys. Rev. A*, 31:3068–3092, May 1985.

[Deg80] Vittorio Degiorgio. Phase shift between the transmitted and the reflected optical fields of a semireflecting lossless mirror is $\pi/2$. *American Journal of Physics*, 48(1):81–81, 1980.

[Dwy13] Sheila E. Dwyer. *Quantum noise reduction using squeezed states in LIGO*. PhD thesis, Massachusetts Institute of Technoloy, 2013.

[Fox06] M. Fox. *Quantum Optics: An Introduction*. Oxford Master Series in Physics. OUP Oxford, 2006.

[Gar05] Floyd M. Gardner. *Phase lock Techniques-3rd edition*. Wiley-Interscience, 3 edition, 2005.

[GK04] C. Gerry and P. Knight. *Introductory Quantum Optics*. Cambridge University Press, 2004.

[Gla63] Roy J. Glauber. Coherent and incoherent states of the radiation field. *Phys. Rev.*, 131:2766–2788, sep 1963.

[Hei27] W. Heisenberg. Über den anschaulichen inhalt der quantentheoretischen kinematik und mechanik. *Zeitschrift fur Physik*, 43:172–198, mar 1927.

[Key] Keysight Technologies. *33521A Function / Arbitrary Waveform Generator, 30 MHz*. `https://www.keysight.com/en/pd-1871159-pn-33521A/`.

[Kha11] Aleksandr Khalaidovski. *Beyond the quantum limit*. PhD thesis, Gottfried Wilhelm Leibniz Universität Hannover, 2011.

[Lou00] R. Loudon. *The Quantum Theory of Light*. OUP Oxford, 2000.

[Mag07] Michele Maggiore. *Gravitational Waves: Volume 1: Theory and Experiments*. Oxford University Press, USA, 2007.

[Mee88] Brian J. Meers. Recycling in laser-interferometric gravitational-wave detectors. *Phys. Rev. D*, 38:2317–2326, Oct 1988.

[Mer70] E. Merzbacher. *Quantum Mechanics*. Wiley, 1970.

[NK03] M.P. Norton and D.G. Karczub. *Fundamentals of Noise and Vibration Analysis for Engineers*. Cambridge University Press, 2003.

[Phy] Physik Instrumente. *PICA Thru Ring Actuators, mod. P-016.00H*. `https://www.physikinstrumente.com/en/?type=5600&downloadUid=881&downloadFileUid=785`.

[Sal14] L. Salasnich. *Quantum Physics of Light and Matter: A Modern Introduction to Photons, Atoms and Many-Body Systems.* UNITEXT for Physics. Springer International Publishing, 2014.

[Sau94] P.R. Saulson. *Fundamentals of Interferometric Gravitational Wave Detectors.* World Scientific, 1994.

[SB88] IEEE Power Engineering Society and IEEE Standards Board. *IEEE Standard Definitions of Physical Quantities for Fundamental Frequency and Time Metrology.* IEEE Std. IEEE, 1988.

[Sta] Stanford Research Systems. *SR770.* FFT Spectrum Analyzer. `http://www.thinksrs.com/products/SR760770.htm`.

[Sto70] D. Stoler. Equivalence classes of minimum uncertainty packets. *Phys. Rev.*, 1:3217–3219, jun 1970.

[Var18] Marco Vardaro. *Toward a fully automated and digitally controlled squeezed vacuum source for gravitational wave detectors.* PhD thesis, Università degli studi di Padova, 2018.

[VCH$^+$06] Henning Vahlbruch, Simon Chelkowski, Boris Hage, Alexander Franzen, Karsten Danzmann, and Roman Schnabel. Coherent control of vacuum squeezing in the gravitational-wave detection band. *Phys. Rev. Lett.*, 97:011101, Jul 2006.

[WKHW86] Ling-An Wu, H. J. Kimble, J. L. Hall, and Huifa Wu. Generation of squeezed states by parametric down conversion. *Phys. Rev. Lett.*, 57:2520–2523, Nov 1986.

[Yat14] R.D. Yates. *Probability and Stochastic Processes: A Friendly Introduction for Electrical and Computer Engineers, 3rd Edition: Third Edition.* Probability and Stochastic Processes: A Friendly Introduction for Electrical and Computer Engineers. John Wiley & Sons, 2014.

[YC83] Horace P. Yuen and Vincent W. S. Chan. Noise in homodyne and heterodyne detection. *Opt. Lett.*, 8(3):177–179, Mar 1983.

[Zei81] A. Zeilinger. General properties of lossless beam splitters in interferometry. *American Journal of Physics*, 49(9):882–883, 1981.

[ZGC$^+$03] T. C. Zhang, K. W. Goh, C. W. Chou, P. Lodahl, and H. J. Kimble. Quantum teleportation of light beams. *Phys. Rev. A*, 67:033802, Mar 2003.